J. Fluid Mech. (2005), *vol.* 540, *pp.* 301–335.
doi:10.1017/S0022112005005884 Printed in the United Kingdom

Receptivity of the compressible mixing layer

By MATTHEW F. BARONE† AND SANJIVA K. LELE

Department of Aeronautics and Astronautics, Stanford University, Stanford, CA 94305, USA

(Received 20 September 2004 and in revised form 2 May 2005)

Receptivity of compressible mixing layers to general source distributions is examined by a combined theoretical/computational approach. The properties of solutions to the adjoint Navier–Stokes equations are exploited to derive expressions for receptivity in terms of the local value of the adjoint solution. The result is a description of receptivity for arbitrary small-amplitude mass, momentum, and heat sources in the vicinity of a mixing-layer flow, including the edge-scattering effects due to the presence of a splitter plate of finite width. The adjoint solutions are examined in detail for a Mach 1.2 mixing-layer flow. The near field of the adjoint solution reveals regions of relatively high receptivity to direct forcing within the mixing layer, with receptivity to nearby acoustic sources depending on the source type and position. Receptivity 'nodes' are present at certain locations near the splitter plate edge where the flow is not sensitive to forcing. The presence of the nodes is explained by interpretation of the adjoint solution as the superposition of incident and scattered fields. The adjoint solution within the boundary layer upstream of the splitter-plate trailing edge reveals a mechanism for transfer of energy from boundary-layer stability modes to Kelvin–Helmholtz modes. Extension of the adjoint solution to the far field using a Kirchhoff surface gives the receptivity of the mixing layer to incident sound from distant sources.

1. Introduction

Receptivity is the process by which external disturbances excite instabilities within a shear flow. The study of receptivity may be divided into two broad classes: receptivity of boundary-layer flows, and receptivity of free shear flows. The importance of receptivity in the study of boundary-layer transition has been recognized for some time. The genesis of various boundary-layer instabilities which lead to transition is described by the receptivity of the flow to environmental disturbances, surface roughness, or actuation of engineering devices. The area of free shear-layer receptivity has received somewhat less attention recently, although it is of critical importance to the study of shear-flow control and modelling of self-resonant flows. As pointed out by Crighton (1985), active control of the fully developed turbulent field in the downstream jet or mixing layer seems impracticable, but control via manipulation of the linear instabilities of the early shear layer may be possible; a theoretical exploration of this idea was made by Ffowcs Williams (2001). Experimental efforts aimed at free shear-flow control using high-frequency and/or high-amplitude actuation (Wiltse & Glezer 1998; Stanek *et al.* 2000; Raman & Kibens 2001) are currently in search of a theory to support the main results. Response of the early mixing layer in these

† Present address: Sandia National Laboratories, PO Box 5800, MS 0825 Albuquerque, NM 87185-0825, USA.

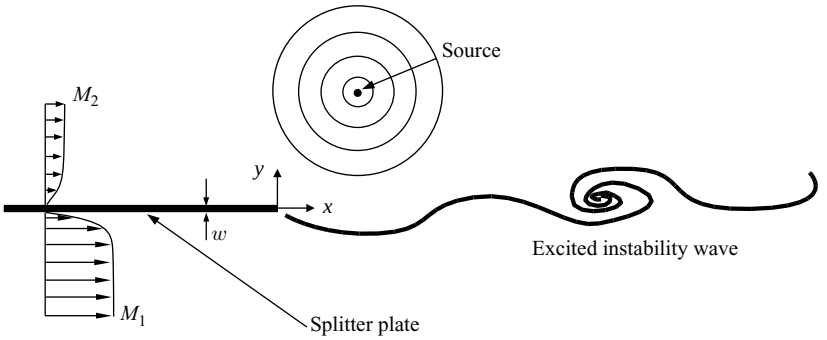

FIGURE 1. Schematic of the mixing-layer receptivity problem.

flows, if not primarily responsible for the control effects, must be well-understood for proper interpretation of the results.

The present paper examines receptivity in a compressible mixing layer. Laboratory experiments on mixing-layer receptivity present numerous difficulties, most notably the inevitable presence of unwanted environmental noise sources in the wind tunnel which may obscure the mechanisms of interest and cause significant facility-to-facility variation in results (Dziomba & Fiedler 1985). The careful numerical treatment explored in this work allows more control over noise and 'experimental' conditions, giving a cleaner picture of the receptivity process. Figure 1 shows a schematic of the present computational model problem. A thin rigid splitter plate separates two co-flowing laminar streams of a compressible gas. The splitter plate extends indefinitely in the upstream direction, but terminates at $x = 0$, creating a free mixing-layer flow downstream. At sufficiently high Reynolds number, the initial mixing layer supports at least one Kelvin–Helmholtz inviscid instability mode. The general receptivity problem considers the response of the mixing layer to incident unsteady disturbances generated by sources of mass, momentum, or heat. For small perturbations to the base flow, the Kelvin–Helmholtz instability is excited over some region downstream of the trailing edge, and it grows in the downstream direction until the point where nonlinear effects become important. The excited mixing layer just described is ubiquitous in flows of engineering interest, including resonant flows such as the cavity and the screeching jet.

1.1. *Previous work on receptivity of free shear flows*

Experimental study of the excitation mechanisms occurring in free shear flows dates back at least as far as the work of Brown (1935), who used smoke visualization techniques to determine that a low-speed jet of air is only sensitive to excitation by sound near the jet exhaust orifice. The advent of linear stability theory led to later experiments on the behaviour of the forced initial shear layer aimed at testing the theoretical predictions. These experiments, and many others (reviewed by Ho & Huerre 1984), focused on the downstream evolution of the shear layer and validation of growth-rate predictions rather than the mechanism for initial instability wave excitation. Over thirty-five years after Brown's observations on receptivity, Morkovin & Paranjape (1971) were the first to demonstrate quantitatively the dominance of a near-edge mechanism in the acoustic excitation of jets. They found that receptivity correlated well with the strength of the acoustic pressure gradient normal to the jet axis near the nozzle lip.

A consistent mathematical model for mixing-layer receptivity was first introduced by Jones & Morgan (1972), who considered the problem of a time-harmonic acoustic line source placed near a subsonic stream separated from still air by a vortex sheet of infinite extent. They found that the solution must include a Kelvin–Helmholtz instability wave component that grows exponentially in the downstream direction in order to satisfy causality. In a subsequent paper, Jones & Morgan (1973) presented a similar analysis for the case of a supersonic stream. Crighton & Leppington (1974) considered the problem of a vortex sheet attached to a rigid half-plane separating still air from a subsonic stream. Using the Wiener–Hopf technique (Noble 1958), they solved for the time-asymptotic mixing-layer response to excitation by a harmonic line source as well as the response to a pulse disturbance. Morgan (1974) considered essentially the same problem, but also treated the supersonic flow case, while Munt (1977) applied a similar model to the round jet configuration. The emphasis of these original vortex-sheet models was placed on the resulting sound field, although expressions were given for the excited instability wave component as residues of a Fourier inversion integral. Of central importance to prediction of receptivity by the models is the unsteady Kutta condition, which represents the action of viscosity near the splitter-plate trailing edge and ensures finite velocities in this region. The validity of the Kutta condition as a physical model of viscous processes near the trailing edge remained in question until detailed analysis of the near-edge region using triple-deck theory (Daniels 1977; Crighton 1985; Peake 1994).

Various other researchers have employed the vortex-sheet model to investigate receptivity of mixing layers and jets. Bechert (1988) reformulated the vortex-sheet problem for the incompressible splitter-plate flow and derived a simple formula for the amplitude of the excited instability wave as a function of the unsteady pressure difference across the splitter plate. In a companion paper, Bechert & Stahl (1988) compared the theoretical predictions of receptivity to carefully controlled experiments, and determined that the vortex-sheet model was valid for Strouhal numbers based on the shear-layer momentum thickness and free-stream velocity of less than about 0.005 (compared with the entire unstable range of Strouhal numbers between zero and 0.04). Kerschen (1996) used the vortex-sheet model to investigate receptivity of compressible shear layers as a function of source location. He found that excitation by sources on the splitter plate adjacent to the flow was more efficient than excitation from the side adjacent to the quiescent fluid. He also found that the receptivity level decreased exponentially with distance from the trailing edge for downstream sources, while for actuators placed on the splitter plate, the receptivity decreased algebraically with distance from the trailing edge. Pal (1996) solved the receptivity problem for a supersonic cylindrical jet with a ring-shaped acoustic source coincident with the vortex sheet surface downstream of the nozzle lip. Bower & Pal (1996) presented results using Pal's model for heated and unheated jets, and reported a general increase in receptivity levels with increasing jet temperature relative to the ambient air.

However, the vortex-sheet model suffers from its simplistic description of the shear layer as a discontinuity between two uniform flow regions. The result of this approximation is a restriction to a band of low frequencies that spans only a small range of the unstable frequencies for a shear layer of finite width. There have been several efforts to develop a receptivity theory that is valid for any temporal frequency. Tam (1978) constructed a theory for the receptivity of a finite-width parallel free shear layer subjected to incident acoustic wave radiation. The Green's function for excitation from the quiescent side of the shear layer is found using transform techniques, and the linear response of the flow is then constructed using the Green's function. The

excited instability wave component is isolated by evaluation of a residue present in the Fourier inversion integral. Tam gave only limited receptivity predictions from his model, but did demonstrate that when the excitation field is given by a beam of sound, the receptivity increased with decreasing beam width. This is a consequence of the wavenumber matching principle (Tam 1986), which states that some portion of both the temporal frequency and spatial scale of the excitation must match that of the instability wave for coupling to occur. Tam's model was applied as the initial part of a quasi-linear model of tone excited jets in Tam & Morris (1985), giving reasonable results for the initial amplitude of the forced instability wave. However, the absence of explicit edge-scattering effects in the model raises questions regarding its applicability for flow geometries containing a scattering surface.

Further theoretical descriptions of finite-width mixing-layer receptivity include the work of Huerre & Monkewitz (1985), who found the response to a point source placed in a parallel, incompressible mixing layer by solving the initial-value problem using transform techniques. Subsequently, Balsa (1988) studied the receptivity of an incompressible free shear layer to excitation by a dipole source using a wave packet analysis. The velocity profile in this study was piecewise linear in order to facilitate evaluation of certain inversion contour integrals. Balsa found that the receptivity increased roughly exponentially with frequency, and that the flow was most sensitive to forcing near the centreline of the shear layer, with a slight bias towards the low-speed side of the layer. The receptivity was also found to be roughly proportional to the velocity difference across the shear layer. Similar conclusions were made regarding the receptivity to perturbations formed from a small oscillating cylinder placed within an incompressible shear layer (Balsa 1993). An attempt to combine a finite-thickness theory for receptivity of Kelvin–Helmholtz instabilities including edge effects was made by Rabchuk (2000), who considered the receptivity of a piecewise linear mixing layer to a point vorticity source placed at the edge of a thin splitter plate. Rabchuk's model sacrifices consistency with a real near-edge flow by assuming a parallel wake/shear layer extending both up- and downstream of the edge. Nevertheless, his model provides useful qualitative information on the response of a low-speed mixing layer across the entire unstable frequency range. Observations include the importance of non-modal and damped-wave components of the solution near the edge, and an increase in receptivity of unstable modes near the neutral frequency.

1.2. *Receptivity prediction using adjoint solutions*

The role of adjoint solutions in linear stability analysis has been recognized at least since the work of Ling & Reynolds (1973) and Saric & Nayfeh (1975), who used the adjoint as part of a solvability condition to compute eigenfunctions of the non-parallel boundary-layer. Adjoint formalism was applied by Tumin & Fedorov (1983, 1984) to investigate the forced response of boundary-layer instabilities to surface vibration. Hill (1995) built upon this approach to the receptivity problem by emphasizing the adjoint eigenfunctions as direct indicators of receptivity. Hill calculated the response to forcing of a parallel, incompressible boundary-layer flow by finding the regular and adjoint eigenfunctions of the Orr–Sommerfeld operator, then applying the biorthogonality property of regular and adjoint modes (Salwen & Grosch 1981) to solve for the amplitude of the excited eigenmode. He also showed that the adjoint-based formula for receptivity is equivalent to the formula derived by Huerre & Monkewitz (1985) for receptivity of a two-dimensional shear layer.

The adjoint approach leads to relatively easy calculation of the receptivity to sources of different types, frequencies and locations, allowing for rapid coverage of the parameter space. Furthermore, in contrast to previous analytical work on receptivity, the mathematical results (in the form of the adjoint eigenfunctions) give the receptivity directly, facilitating physical interpretation of the results. The adjoint approach was extended to non-parallel incompressible boundary-layer flows by Hill (1997), Dobrinsky & Collis (2000) and Airiau (2000). Luchini & Bottaro (1998) recognized that the adjoint operator could be used to compute amplitudes of modes that only posess a distinctive propagative behaviour well-downstream of the excitation location. They applied adjoint solutions of the boundary-layer equations to compute receptivity of Görtler vortices.

Application of adjoint methods to free shear flows has been somewhat limited; Suzuki (2001) applied the adjoint approach in calculating the instability wave component of the Green's function for an inviscid, compressible free shear layer, but considered only a single set of flow and excitation conditions. In a related application to jet aeroacoustics, Tam & Aurialt (1998) applied adjoint solutions to study mean flow refraction of sound through a jet shear layer.

We build on the adjoint approach to receptivity prediction by considering its application to the mixing layer with the splitter plate present. The inhomogeneity introduced by the splitter plate complicates a purely theoretical treatment, but the appropriate adjoint problem may still be formulated and solved computationally. This results in solution of an adjoint scattering problem; the incident and scattered adjoint fields each have direct physical interpretations relating to receptivity of the flow. Furthermore, the analysis is only constrained by the assumption of linearity, and is not restricted to particular frequency bands or to certain limits of the flow parameters.

The following section gives the theoretical basis for the adjoint approach to receptivity prediction. The governing equations are presented, including the adjoint equations. The primary result of the analysis is an expression for the receptivity of a particular instability mode in terms of an adjoint solution and an arbitrary source distribution. Section 3 begins with a brief explanation of the numerical techniques employed to solve the adjoint equations and then examines, in detail, the receptivity of a supersonic mixing layer. The final section of the paper offers some conclusions regarding the present work.

2. Receptivity prediction using adjoint equations

2.1. *The regular governing equations*

Consider a nominally steady mixing-layer flow that is perturbed by a source generating small-amplitude disturbances. A general flow variable χ is represented by the sum of a steady mean value $\bar{\chi}$ and a fluctuating component $\tilde{\chi}$. Substitution of this form into the Navier–Stokes equations for compressible flow and subsequent linearization in the fluctuating terms yield the linearized Navier–Stokes equations (LNS) in non-dimensional form:

$$\frac{\partial \tilde{\rho}}{\partial t} + \bar{u}_k \frac{\partial \tilde{\rho}}{\partial x_k} + \bar{\rho} \frac{\partial \tilde{u}_k}{\partial x_k} + \tilde{u}_k \frac{\partial \bar{\rho}}{\partial x_k} + \tilde{\rho} \frac{\partial \bar{u}_k}{\partial x_k} = \tilde{s}_\rho, \tag{2.1}$$

$$\frac{\partial \tilde{u}_i}{\partial t} + \bar{u}_k \frac{\partial \tilde{u}_i}{\partial x_k} + \left(\tilde{u}_k + \frac{\tilde{\rho}}{\bar{\rho}} \bar{u}_k \right) \frac{\partial \bar{u}_i}{\partial x_k} + \frac{1}{\bar{\rho}} \frac{\partial \tilde{p}}{\partial x_i} = \frac{M_1}{\bar{\rho} Re} \frac{\partial \tilde{\tau}_{ik}}{\partial x_k} + \tilde{s}_{u_i}, \tag{2.2}$$

$$\frac{\partial \tilde{T}}{\partial t} + \bar{u}_k \frac{\partial \tilde{T}}{\partial x_k} + \left(\tilde{u}_k + \frac{\tilde{\rho}}{\bar{\rho}} \bar{u}_k \right) \frac{\partial \bar{T}}{\partial x_k} + \frac{\gamma}{\bar{\rho}} \left[\bar{p} \frac{\partial \tilde{u}_k}{\partial x_k} + \tilde{p} \frac{\partial \bar{u}_k}{\partial x_k} \right] = \frac{\gamma M_1}{\bar{\rho} Re} \tilde{\Phi} - \frac{\gamma M_1}{\bar{\rho} Re Pr} \frac{\partial \tilde{q}_k}{\partial x_k} + \tilde{s}_T. \quad (2.3)$$

The fluid velocity vector is given by u_i, while the thermodynamic state is described by the pressure p, density ρ and temperature T. The forms for the linear viscous stress tensor $\tilde{\tau}_{ik}$, heat flux $\tilde{q}_i$, and the irreversible linear dissipation term $\tilde{\Phi}$ are given in the Appendix. The linearized form of the ideal gas law, also given in the Appendix, closes the equations. The length, velocity and time scales used for non-dimensionalization are the fast-stream boundary-layer momentum thickness θ_1^*, the isentropic speed of sound c_1^*, and the ratio θ_1^*/c_1^*, respectively. Density is non-dimensionalized by the reference quantity ρ_1^*, pressure by $\rho_1^* c_1^{*2}$, and temperature by $(\gamma - 1)T_1^*$. Non-dimensional parameters appearing in (2.1)–(2.3) are the fast stream Mach number M_1, the Reynolds number $Re = \rho_1^* u_1^* \theta_1^* / \mu_1^*$, the Prandtl number $Pr = \mu_1^* C_p / k_1^*$ and the ratio of specific heats $\gamma = C_p / C_v$. The viscosity μ is related to temperature using the power law relationship $\mu(T) = ((\gamma - 1)T)^{2/3}$, which is valid for moderate temperatures.

The terms $\tilde{s}_\rho$, $\tilde{s}_{u_i}$ and $\tilde{s}_T$, added to the right-hand sides of the equations, represent the presence of small-amplitude externally applied sources. The rate of volumetric mass addition is $\tilde{s}_\rho$, while the rate of volumetric heat addition per unit mass is $\tilde{s}_T$. The term $\tilde{s}_{u_i}$ represents a body-force distribution; multiplying by the mean density $\bar{\rho}$ transforms $\tilde{s}_{u_i}$ to a linear momentum source. These source terms are one mechanism for providing the input excitation in the receptivity analysis to follow. We note that the present source terms are simply related to source terms implied in the original nonlinear equations.

Equations (2.1)–(2.3) may be written in compact vector notation,

$$\frac{\partial \tilde{\boldsymbol{U}}}{\partial t} + \boldsymbol{L}(\tilde{\boldsymbol{U}}) = \tilde{\boldsymbol{s}}, \quad (2.4)$$

where, in two dimensions,

$$\tilde{\boldsymbol{U}}(\boldsymbol{x}, t) = [\tilde{\rho} \quad \tilde{u} \quad \tilde{v} \quad \tilde{T}]^T, \qquad \tilde{\boldsymbol{s}}(\boldsymbol{x}, t) = [\tilde{s}_\rho \quad \tilde{s}_u \quad \tilde{s}_v \quad \tilde{s}_T]^T. \quad (2.5)$$

2.2. *Adjoint equations and the Euler–Lagrange identity*

The adjoint equations are derived by taking the dot product of a smooth vector field $\boldsymbol{V}^\dagger(\boldsymbol{x}, t)$ and (2.4). After repeated application of integration by parts, we are left with the following relation, called the *Euler–Lagrange identity*:

$$\tilde{\boldsymbol{U}} \cdot \left(\frac{\partial \boldsymbol{V}^\dagger}{\partial t} + \boldsymbol{L}^\dagger(\boldsymbol{V}^\dagger) \right) + \boldsymbol{V}^\dagger \cdot \tilde{\boldsymbol{s}} = \frac{\partial}{\partial t} \varrho(\tilde{\boldsymbol{U}}, \boldsymbol{V}^\dagger) + \nabla \cdot \boldsymbol{J}(\tilde{\boldsymbol{U}}, \boldsymbol{V}^\dagger). \quad (2.6)$$

At this point $\boldsymbol{V}^\dagger(\boldsymbol{x}, t)$ is identified as the adjoint field, and $\partial \boldsymbol{V}^\dagger / \partial t + \boldsymbol{L}^\dagger(\boldsymbol{V}^\dagger) = 0$ is defined as the system of homogenous adjoint equations that govern the behaviour of $\boldsymbol{V}^\dagger$. The quantities $\boldsymbol{J}$ and ϱ will be defined in due course. The elements of $\boldsymbol{V}^\dagger$ in two dimensions are labelled as follows,

$$\boldsymbol{V}^\dagger = [\rho^\dagger \quad u^\dagger \quad v^\dagger \quad T^\dagger]^T, \quad (2.7)$$

although the adjoint variables have quite different physical meanings from their regular counterparts. For convenience, we also introduce an adjoint 'pressure', defined as

$$p^\dagger = \bar{\rho} \left(\rho^\dagger + \bar{c}^2 T^\dagger \right). \quad (2.8)$$

The homogenous adjoint equations written out in full are

$$\frac{\partial \rho^\dagger}{\partial t} + \bar{u}_k \frac{\partial \rho^\dagger}{\partial x_k} - \bar{u}_k \frac{\partial \bar{u}_i}{\partial x_k} u_i^\dagger + \frac{\gamma - 1}{\gamma} \bar{T} \frac{\partial u_k^\dagger}{\partial x_k} - \left[\bar{u}_k \frac{\partial \bar{T}}{\partial x_k} + (\gamma - 1) \bar{T} \frac{\partial \bar{u}_k}{\partial x_k} \right] T^\dagger = 0, \tag{2.9}$$

$$\frac{\partial u_i^\dagger}{\partial t} + \bar{u}_k \frac{\partial u_i^\dagger}{\partial x_k} - u_k^\dagger \frac{\partial \bar{u}_k}{\partial x_i} + \frac{1}{\bar{\rho}} \frac{\partial p^\dagger}{\partial x_i} - \frac{\partial \bar{T}}{\partial x_i} T^\dagger - \frac{\rho^\dagger}{\bar{\rho}} \frac{\partial \bar{\rho}}{\partial x_i} = \frac{M_1}{\bar{\rho} Re} \frac{\partial \tau_{ik}^\dagger}{\partial x_k}, \tag{2.10}$$

$$\frac{\partial T^\dagger}{\partial t} + \bar{u}_k \frac{\partial T^\dagger}{\partial x_k} + (\gamma - 1) \left(\frac{1}{\gamma} \frac{\partial u_k^\dagger}{\partial x_k} - \frac{\partial \bar{u}_k}{\partial x_k} T^\dagger \right) = \frac{M_1}{\bar{\rho} Re} \Phi^\dagger - \frac{\gamma M_1}{\bar{\rho} Re Pr} \bar{\mu} \frac{\partial^2 T^\dagger}{\partial x_k^2}, \tag{2.11}$$

where

$$\tau_{ik}^\dagger = 2\gamma T^\dagger \bar{\tau}_{ik} - \left(\bar{\mu} \left[\frac{\partial u_i^\dagger}{\partial x_k} + \frac{\partial u_k^\dagger}{\partial x_i} \right] + \bar{\lambda} \frac{\partial u_j^\dagger}{\partial x_j} \delta_{ik} \right) \tag{2.12}$$

and

$$\Phi^\dagger = \frac{\partial \bar{\mu}}{\partial \bar{T}} \left(\frac{\partial \bar{u}_i}{\partial x_k} + \frac{\partial \bar{u}_k}{\partial x_i} \right) \frac{\partial u_i^\dagger}{\partial x_k} + \frac{\partial \bar{\lambda}}{\partial \bar{T}} \frac{\partial \bar{u}_i}{\partial x_i} \frac{\partial u_k^\dagger}{\partial x_k} - \gamma \left(\frac{\partial \bar{u}_i}{\partial x_k} \left[\frac{\partial \bar{u}_i}{\partial x_k} + \frac{\partial \bar{u}_k}{\partial x_i} \right] \mu^\dagger + \left[\frac{\partial \bar{u}_k}{\partial x_k} \right]^2 \lambda^\dagger \right). \tag{2.13}$$

Examination of the dissipative terms in (2.10) and (2.11) reveals that the adjoint equations should be integrated backwards in time in order to maintain well-posedness.

Returning now to the Euler–Lagrange identity (2.6), the right-hand side contains two terms: a time derivative term, and a divergence term. The scalar variable ϱ appearing in the time derivative term is given by

$$\varrho(\tilde{\boldsymbol{U}}, \boldsymbol{V}^\dagger) = \rho^\dagger \tilde{\rho} + \bar{\rho} u_i^\dagger \tilde{u}_i + \bar{\rho} T^\dagger \tilde{T}. \tag{2.14}$$

$\boldsymbol{J}(\tilde{\boldsymbol{U}}, \boldsymbol{V}^\dagger)$, which appears in the divergence term, is called the *bilinear concomitant*. It contains weighted sums of products of the elements of $\tilde{\boldsymbol{U}}$ and $\boldsymbol{V}^\dagger$ and their spatial derivatives, with the kth element of $\boldsymbol{J}$ given by

$$\begin{aligned} \boldsymbol{J}_k = {} & \bar{u}_k (\tilde{\rho} \rho^\dagger + \bar{\rho} [u_i^\dagger \tilde{u}_i + \tilde{T} T^\dagger]) + \tilde{p} u_k^\dagger + p^\dagger \tilde{u}_k \\ & + \frac{M_1}{Re} \left\{ -\tilde{u}_i \tau_{ik}^\dagger - u_i^\dagger \tilde{\tau}_{ik} + \frac{\gamma}{Pr} \left[\bar{\mu} \left(\tilde{T} \frac{\partial T^\dagger}{\partial x_k} - T^\dagger \frac{\partial \tilde{T}}{\partial x_k} \right) - \frac{\partial \bar{\mu}}{\partial x_k} \tilde{T} T^\dagger \right] \right\}. \end{aligned} \tag{2.15}$$

2.3. *Modal decomposition and biorthogonality*

Investigations of the stability of parallel shear flows often introduce a modal description of the unsteady disturbances. The stability of a particular mode is then described through specification of its complex wavenumber. Mixing-layer flows at reasonably high Reynolds number are not parallel, but, far enough downstream from the near-edge region, the mean flow changes slowly in the streamwise direction relative to the oscillatory behaviour of the unsteady disturbances of interest. In a real laminar mixing layer, instabilities eventually grow to large amplitudes and lead to nonlinear thickening of the layer and transition to turbulence. The present analysis assumes that there exists a finite region upstream of this nonlinear region where the mean flow is laminar and not directly influenced by the downstream flow. In this region the following regular and adjoint disturbance forms may be assumed,

$$\tilde{\boldsymbol{U}}(x, y, z, t) = \hat{\boldsymbol{U}}(x, y) \exp(\mathrm{i}(\omega t - \beta z)), \qquad \boldsymbol{V}^\dagger(x, y, z, t) = \hat{\boldsymbol{V}}^\dagger(x, y) \exp(\mathrm{i}(\omega t - \beta z)), \tag{2.16}$$

where

$$\hat{\boldsymbol{U}}(x,y)=\hat{\boldsymbol{\phi}}(x,y)\exp\left(-\mathrm{i}\int_{x_a}^{x}\alpha(x')\mathrm{d}x'\right),\quad \hat{\boldsymbol{V}}^{\dagger}(x,y)=\hat{\boldsymbol{\phi}}^{\dagger}(x,y)\exp\left(\mathrm{i}\int_{x_b}^{x}\alpha^{\dagger}(x')\,\mathrm{d}x'\right). \tag{2.17}$$

The complex wavenumbers in the streamwise and spanwise directions are given by α and β, respectively, while ω is the given real temporal frequency. The 'eigenfunctions' $\hat{\boldsymbol{\phi}}$ and $\hat{\boldsymbol{\phi}}^{\dagger}$ are required to change slowly in x relative to the variations due to the exponential factor. We also define the splitting such that $\alpha(x)=\alpha^{\dagger}(x)$ for regular/adjoint mode pairs. This disturbance form is the basis for derivation of the parabolized stability equations (PSE), which have been used to predict successfully streamwise evolution of shear-layer instability modes in non-parallel flows (e.g. Day, Mansour & Reynolds 2001).

Homogenous regular solutions for a particular ω are written as a combination of discrete and continuous modes:

$$\tilde{\boldsymbol{U}}(x,y,t)=\int_{-\infty}^{\infty}\left[\sum_{n=1}^{N(\omega)}a_n\hat{\boldsymbol{\phi}}_n(x,y)\exp\left(\mathrm{i}\left(\omega t-\int\alpha_n(x')\,\mathrm{d}x'\right)\right)\right.$$
$$\left.+\sum_{\nu=1}^{3}\int_0^{\infty}b_k^{(\nu)}\hat{\boldsymbol{\phi}}_k^{(\nu)}(x,y)\exp\left(\mathrm{i}\left(\omega t-\int\alpha_k^{(\nu)}(x')\,\mathrm{d}x'\right)\right)\mathrm{d}k\right]\exp(-\mathrm{i}\beta z)\,\mathrm{d}\beta. \tag{2.18}$$

The discrete mode amplitudes are given by a_n while the amplitude of the kth continuous mode of the ν branch is $b_k^{(\nu)}$. For homogenous ($\tilde{\boldsymbol{s}}=0$) time harmonic solutions to the regular and adjoint equations, the Euler–Lagrange identity (2.6) integrated in the y direction becomes

$$\frac{\partial}{\partial x}[\hat{\boldsymbol{U}},\hat{\boldsymbol{V}}^{\dagger}]=0, \tag{2.19}$$

with the following inner product definition,

$$[\boldsymbol{f},\boldsymbol{g}]\equiv\int_{-\infty}^{+\infty}\boldsymbol{J}(\boldsymbol{f},\boldsymbol{g})\cdot\boldsymbol{e}_x\,\mathrm{d}y. \tag{2.20}$$

Substitution of (2.17) into (2.19) yields

$$[\hat{\boldsymbol{U}},\hat{\boldsymbol{V}}^{\dagger}]=C[\hat{\boldsymbol{\phi}},\hat{\boldsymbol{\phi}}^{\dagger}]\exp\left(-\int_{x_a}^{x}\mathrm{i}\Delta_{\alpha}(x')\,\mathrm{d}x'\right)=\text{const.}\qquad(\Delta_{\alpha}=\alpha-\alpha^{\dagger}) \tag{2.21}$$

where $C=\exp(\int_{x_b}^{x_a}\mathrm{i}\alpha^{\dagger}(x')\,\mathrm{d}x')$ is a definite integral that is equal to a constant for fixed x_a and x_b. If $\alpha=\alpha^{\dagger}$ then $[\hat{\boldsymbol{\phi}},\hat{\boldsymbol{\phi}}^{\dagger}]$ equals a constant, since the exponential term becomes unity. In this case, we choose the normalization constant to be $[\hat{\boldsymbol{\phi}},\hat{\boldsymbol{\phi}}^{\dagger}]=1$ for convenience. If $\alpha\neq\alpha^{\dagger}$ then $[\hat{\boldsymbol{\phi}},\hat{\boldsymbol{\phi}}^{\dagger}]$ must either vary exponentially with x or equal zero. Since by construction any exponential behaviour of the eigenfunctions has been explicitly factored out, $[\hat{\boldsymbol{\phi}},\hat{\boldsymbol{\phi}}^{\dagger}]$ must equal zero. Therefore, the following biorthogonality relations, derived originally by Salwen & Grosch (1981) for parallel flow, hold in the weakly non-parallel case as well:

$$[\hat{\boldsymbol{\phi}}_n,\hat{\boldsymbol{\phi}}_m^{\dagger}]=\delta_{nm}\quad(n,m=1,\ldots,N(\omega)), \tag{2.22a}$$

$$\left[\hat{\boldsymbol{\phi}}_k^{(\nu)},\hat{\boldsymbol{\phi}}_n^{\dagger}\right]=\left[\hat{\boldsymbol{\phi}}_n,\hat{\boldsymbol{\phi}}_k^{\dagger(\nu)}\right]=0\quad(n=1,\ldots,N(\omega),\quad\nu=1,\ldots,3), \tag{2.22b}$$

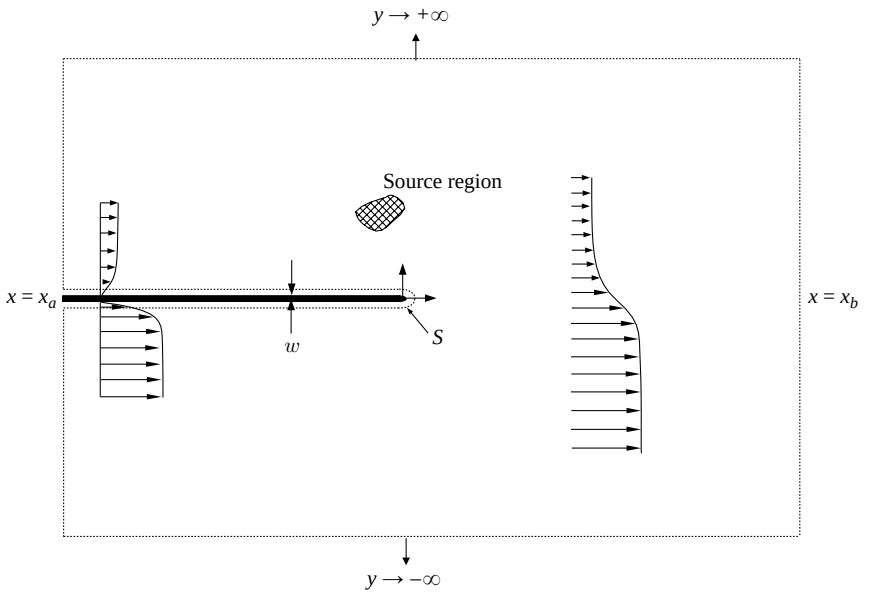

FIGURE 2. Control volume V for integration of the Euler–Lagrange identity. The surface S is shown displaced from the actual splitter-plate surface for clarity.

$$\left[\hat{\boldsymbol{\phi}}_k^{(\nu)}, \hat{\boldsymbol{\phi}}_{k'}^{\dagger(\mu)}\right] = \delta(k - k')\delta_{\nu\mu} \quad (\mu, \nu = 1, \ldots, 3). \tag{2.22c}$$

The essential features of this argument are due to Dobrinsky & Collis (2000), who successfully applied the biorthogonality condition to predict receptivity of weakly non-parallel incompressible boundary layers.

The spatial modes under consideration may propagate in the downstream ($+x$) direction or the upstream ($-x$) direction depending on whether their group velocity $v_g \equiv d\omega/d\alpha$ is positive or negative. If v_g is positive, then the regular eigenmode propagates downstream. However, the corresponding adjoint eigenmode propagates in the upstream direction, i.e. $v_g = -v_g^\dagger$ (Hill 1995). This is due to the reversed time dependence of adjoint solutions discussed in § 2.2. If $v_g < 0$, the regular eigenmode propagates in the upstream direction while the adjoint eigenmode propagates downstream. Likewise, a regular unstable mode with positive $\alpha_i \equiv \mathrm{Imag}(\alpha)$ grows in the downstream direction while the related adjoint instability mode grows upstream.

2.4. *Receptivity prediction*

We are now in a position to derive an expression for receptivity using adjoint solutions. This is accomplished by integration of the Euler–Lagrange identity (2.6) over an appropriate control volume, followed by application of the biorthogonality properties derived in the previous section.

We begin by substituting a solution to the regular LNS equations (with source terms) and an adjoint solution into (2.6) and integrating over the control volume V pictured in figure 2. The cut rectangular control volume chosen extends far upstream and downstream of any sources, wraps around the splitter plate of width w, and has upper and lower boundaries that are pushed to $y = \pm\infty$. We shall see that the adjoint instability eigenmode serves as a filter to the forced regular solution, allowing the extraction of the unstable regular eigenmode amplitude of interest (Hill 1995). This mathematical property depends, however, on the proper choice of boundary

conditions for the adjoint problem. We define a particular solution to the adjoint equations in which the instability eigenfunction (the mth mode) is specified at the downstream boundary as *the only upstream travelling adjoint disturbance*. This adjoint solution consists of the adjoint eigenmode plus scattered waves that result from the eigenmode impinging on the splitter plate. Its form at the boundaries x_a and x_b assumes the following modal decomposition for weakly parallel flow,

$$\begin{aligned}\boldsymbol{V}_f^\dagger(x,y,t) = {}& \hat{\boldsymbol{\phi}}_m^\dagger(x,y)\exp\left(\mathrm{i}\int_{x_b}^{x}\alpha_m^\dagger(x')\,\mathrm{d}x'\right)\exp(-\mathrm{i}(\omega t-\beta_m z))\\ &+\int_{-\infty}^{\infty}\left[\sum_{n\neq m}a_n^\dagger\hat{\boldsymbol{\phi}}_n^\dagger(x,y)\exp\left(-\mathrm{i}\left(\omega t-\int\alpha_n^\dagger(x')\,\mathrm{d}x'\right)\right)\right.\\ &\left.+\sum_{\nu=1}^{3}\int_0^\infty b_k^{\dagger(\nu)}\hat{\boldsymbol{\phi}}_k^{\dagger(\nu)}(x,y)\exp\left(-\mathrm{i}\left(\omega t-\int\alpha_k^{\dagger(\nu)}(x')\,\mathrm{d}x'\right)\right)\mathrm{d}k\right]\\ &\times\exp(\mathrm{i}\beta z)\,\mathrm{d}\beta. \end{aligned}\tag{2.23}$$

The adjoint solution satisfies a radiation boundary condition precluding any modes propagating from the far field into the domain (as time is reversed), except for the prescribed instability mode. At x_a we only have regular and adjoint modes propagating upstream,

$$\frac{\mathrm{d}\omega}{\mathrm{d}\alpha}<0,\quad \frac{\mathrm{d}\omega}{\mathrm{d}\alpha^\dagger}<0,\quad x=x_a.\tag{2.24}$$

At x_b, the only mode propagating upstream is the imposed adjoint instability mode, giving

$$\frac{\mathrm{d}\omega}{\mathrm{d}\alpha}>0,\quad \left.\frac{\mathrm{d}\omega}{\mathrm{d}\alpha^\dagger}\right|_{n\neq m}>0,\quad x=x_b.\tag{2.25}$$

Substituting $\tilde{\boldsymbol{U}}$ and $\boldsymbol{V}_f^\dagger$ into the Euler–Lagrange identity (2.6) and integrating over the control volume gives

$$\begin{aligned}&[\hat{\boldsymbol{U}},\hat{\boldsymbol{V}}_f^\dagger]_{x_b}+\int_{-\infty}^{-w/2}\boldsymbol{J}(\hat{\boldsymbol{U}}(x_a,y),\hat{\boldsymbol{V}}_f^\dagger(x_a,y))\cdot\boldsymbol{e}_x\,\mathrm{d}y+\int_{w/2}^{\infty}\boldsymbol{J}(\hat{\boldsymbol{U}}(x_a,y),\hat{\boldsymbol{V}}_f^\dagger(x_a,y))\cdot\boldsymbol{e}_x\,\mathrm{d}y\\ &\quad-\int_{x_a}^{x_b}\boldsymbol{J}(\hat{\boldsymbol{U}}(x,\infty),\hat{\boldsymbol{V}}_f^\dagger(x,\infty))\cdot\boldsymbol{e}_y\,\mathrm{d}x+\int_{x_a}^{x_b}\boldsymbol{J}(\hat{\boldsymbol{U}}(x,-\infty),\hat{\boldsymbol{V}}_f^\dagger(x,-\infty))\cdot\boldsymbol{e}_y\,\mathrm{d}x\\ &=\int_V\hat{\boldsymbol{s}}\cdot\hat{\boldsymbol{V}}_f^\dagger\,\mathrm{d}V-\int_S\boldsymbol{J}(\hat{\boldsymbol{U}},\hat{\boldsymbol{V}}_f^\dagger)\cdot\boldsymbol{n}\,\mathrm{d}S,\end{aligned}\tag{2.26}$$

where $\boldsymbol{n}$ is the outward unit normal vector on the splitter plate surface and the last integral is evaluated along the splitter plate surface in the direction from $(-\infty,-w/2)$ to $(-\infty,+w/2)$. In the present treatment, we require quasi-parallel flow conditions (which are, in general, different) to exist at x_a and x_b. However, we note that (2.26) is an exact result for a general non-parallel flow in the region $x_a<x<x_b$.

Radiating far-field forms for the regular and adjoint solutions were presented in Barone (2003). It was shown in Barone (2003) that the upper and lower far-field integrals in (2.26) are $O(|y|^{-1/2})$ as $y\to\pm\infty$ and therefore vanish. For the integrals over the upstream boundary layers, we define two new inner products identical to (2.20), except for the range of integration. These new inner products are $[\boldsymbol{f},\boldsymbol{g}]^+$ for integration from $y=w/2$ to ∞ and $[\boldsymbol{f},\boldsymbol{g}]^-$ for integration from $y=-\infty$ to $-w/2$. Solution modes at x_a satisfy the biorthogonality conditions (2.22) using these

boundary-layer inner products. After application of the far-field conditions, we are then left with

$$[\hat{\boldsymbol{U}}, \hat{\boldsymbol{V}}_f^\dagger]_{x_b} + [\hat{\boldsymbol{U}}, \hat{\boldsymbol{V}}_f^\dagger]_{x_a}^- + [\hat{\boldsymbol{U}}, \hat{\boldsymbol{V}}_f^\dagger]_{x_a}^+ = \int_V \hat{\boldsymbol{s}} \cdot \hat{\boldsymbol{V}}_f^\dagger \, \mathrm{d}V - \int_S \boldsymbol{J}(\hat{\boldsymbol{U}}, \hat{\boldsymbol{V}}_f^\dagger) \cdot \boldsymbol{n} \, \mathrm{d}S. \tag{2.27}$$

We now substitute the decomposition (2.18) and (2.23) into (2.27). The summations over modes are brought outside of the inner products, resulting in integrands containing inner products of individual solution modes. At $x = x_a$, the wave propagation conditions (2.24) imply that no regular/adjoint mode pairs co-exist there. Biorthogonality (2.22) thus dictates that the inner products of these modes vanish. Likewise, the inner products at $x = x_b$ are all zero except for the one involving the instability mode pair, which evaluates to $a_m(x_b)[\hat{\boldsymbol{\phi}}_m, \hat{\boldsymbol{\phi}}_m^\dagger]$. We are then left with a useful formula for the regular instability mode amplitude,

$$a_m(x_b) = \frac{\displaystyle\int_V \hat{\boldsymbol{s}} \cdot \hat{\boldsymbol{V}}_f^\dagger \, \mathrm{d}V - \int_S \boldsymbol{J}(\hat{\boldsymbol{U}}, \hat{\boldsymbol{V}}_f^\dagger) \cdot \boldsymbol{n} \, \mathrm{d}S}{[\hat{\boldsymbol{\phi}}_m, \hat{\boldsymbol{\phi}}_m^\dagger]}. \tag{2.28}$$

The first term in the numerator of (2.28) represents the receptivity to the source distribution described by $\hat{\boldsymbol{s}}$. It is the projection of the source term onto the adjoint solution, and because of this, each element of the adjoint solution vector corresponds to excitation by a point source of a given type. For example, take the case of a point mass source, $\hat{\boldsymbol{s}} = [\delta(\boldsymbol{x} - \boldsymbol{x}_0)\ 0\ 0\ 0]^T$. The amplitude of the excited instability wave is simply $\hat{\rho}^\dagger(\boldsymbol{x}_0)/[\hat{\boldsymbol{\phi}}_m, \hat{\boldsymbol{\phi}}_m^\dagger]$, or the properly normalized value of the adjoint density evaluated at the source location. Likewise, the adjoint velocities are related to point body forces and the adjoint temperature is related to a point volumetric heat source.

By application of homogenous regular solid-wall boundary conditions along with appropriate solid-wall boundary conditions for the adjoint equations, the integrand of the solid-surface integral in (2.28) is made to vanish. The inviscid adjoint boundary condition is analogous to the non-penetration condition for the regular equations, and is expressed as

$$\hat{\boldsymbol{u}}^\dagger \cdot \boldsymbol{n} = 0. \tag{2.29}$$

For viscous flows the adjoint wall boundary conditions involve setting the adjoint velocity components to zero at the wall and either setting the adjoint temperature disturbance to zero (for the isothermal wall condition) or setting the wall-normal adjoint temperature gradient to zero (for the adiabatic wall condition). Note that we are referring to the temperature disturbance wall boundary conditions; the mean temperature boundary condition does not affect the choice of adjoint temperature boundary condition.

Alternatively, the surface boundary integral in (2.28) illustrates how the adjoint solution and its spatial derivatives on the splitter plate determine the receptivity to nonhomogeneous wall boundary conditions. Consider an adiabatic wall, where the adjoint wall boundary conditions for viscous flow are $\hat{u}^\dagger = \hat{v}^\dagger = 0$, $\partial \hat{T}^\dagger / \partial n = 0$. Unsteady suction/blowing normal to the wall surface is introduced by application of the boundary condition $\hat{\boldsymbol{u}} \cdot \boldsymbol{n} = \hat{v}_b$, where $\hat{v}_b$ is the amplitude of the applied boundary velocity. This introduces the following non-zero component to $\boldsymbol{J}(\hat{\boldsymbol{U}}, \hat{\boldsymbol{V}}_f^\dagger) \cdot \boldsymbol{n}$:

$$\{\boldsymbol{J}(\hat{\boldsymbol{U}}, \hat{\boldsymbol{V}}_f^\dagger) \cdot \boldsymbol{n}\}_{blowing} = \hat{v}_b \left(\hat{p}^\dagger + \frac{M}{Re} \hat{\tau}_{nn}^\dagger \right). \tag{2.30}$$

Source description	Adjoint expression for receptivity
Point mass source, $\hat{s}_\rho = \delta(\boldsymbol{x} - \boldsymbol{x}_0)$	$\hat{\rho}^\dagger(\boldsymbol{x}_0)$
Point body force, $\hat{s}_{u_i} = \delta(\boldsymbol{x} - \boldsymbol{x}_0)$	$\hat{u_i}^\dagger(\boldsymbol{x}_0)$
Point volumetric heat source, $\hat{s}_T = \delta(\boldsymbol{x} - \boldsymbol{x}_0)$	$\hat{T}^\dagger(\boldsymbol{x}_0)$
Surface normal unsteady blowing, $\hat{v} = \hat{v}_b \delta(\boldsymbol{x} - \boldsymbol{x}_0)$	$\hat{v}_b \left(\hat{p}(\boldsymbol{x}_0)^\dagger + \dfrac{M}{Re} \hat{\tau}_{nn}^\dagger(\boldsymbol{x}_0) \right)$
Surface unsteady heating, $\hat{T} = \hat{T}_b \delta(\boldsymbol{x} - \boldsymbol{x}_0)$	$\dfrac{\gamma M}{Re\, Pr} \bar{\mu} \dfrac{\partial \hat{T}^\dagger}{\partial n}(\boldsymbol{x}_0) \hat{T}_b$

TABLE 1. Physical source description and associated adjoint expression for determining receptivity.

The adjoint terms in (2.30) constitute an adjoint 'stress' with an inviscid part given by the adjoint pressure and a viscous component given by $(M/Re)\hat{\tau}_{nn}^\dagger$, where $\hat{\tau}_{nn}^\dagger$ is the adjoint normal viscous stress in the wall normal direction. For an isothermal wall, the adjoint pressure in (2.30) is replaced by $\bar{\rho}\hat{\rho}^\dagger$. Unsteady heating of the surface resulting in a surface temperature fluctuation $\hat{T}_b$ introduces the following non-zero contribution to $\boldsymbol{J}(\hat{\boldsymbol{U}}, \hat{\boldsymbol{V}}_f^\dagger) \cdot \boldsymbol{n}$:

$$\{ \boldsymbol{J}(\hat{\boldsymbol{U}}, \hat{\boldsymbol{V}}_f^\dagger) \cdot \boldsymbol{n} \}_{heating} = \frac{\gamma M}{Re\ Pr} \bar{\mu} \frac{\partial \hat{T}^\dagger}{\partial n} \hat{T}_b. \tag{2.31}$$

The sensitivity to unsteady wall heating is determined by the wall-normal adjoint temperature gradient. A summary of the physical source mechanisms, and the associated adjoint expressions for receptivity, is given in table 1.

Next consider the case where there are no sources near the plate edge, but instead the excitation comes from an incident disturbance field $\hat{\boldsymbol{U}}_i(x, y)$ originating far upstream from the trailing edge and composed of downstream travelling normal modes. This type of excitation model may be convenient when considering the response to incident disturbances with a known form, such as trapped waves within the boundary layer or vortical gusts, rather than to a particular source distribution. In this case, (2.26) reduces to

$$a_m(x_b) = -\frac{\displaystyle\int_{-\infty}^{-w/2} \boldsymbol{J}(\hat{\boldsymbol{U}}_i(x_a, y), \hat{\boldsymbol{V}}_f^\dagger(x_a, y)) \cdot \boldsymbol{e}_x \, \mathrm{d}y + \int_{w/2}^{\infty} \boldsymbol{J}(\hat{\boldsymbol{U}}_i(x_a, y), \hat{\boldsymbol{V}}_f^\dagger(x_a, y)) \cdot \boldsymbol{e}_x \, \mathrm{d}y}{[\hat{\boldsymbol{\phi}}_m, \hat{\boldsymbol{\phi}}_m^\dagger]}. \tag{2.32}$$

This gives the triggered instability wave amplitude in terms of inner products of the adjoint field with the incident field evaluated at some location x_a upstream of the edge. Similarly, for sound generated from far downstream and propagating in the upstream direction with incident field $\hat{\boldsymbol{U}}_i(x, y)$, the instability wave amplitude is given by

$$a_m(x_b) = -\frac{[\hat{\boldsymbol{U}}_i, \hat{\boldsymbol{V}}_f^\dagger]_{x_b}}{[\hat{\boldsymbol{\phi}}_m, \hat{\boldsymbol{\phi}}_m^\dagger]}. \tag{2.33}$$

The adjoint solution also enables prediction of receptivity to acoustic disturbances originating far from the plate edge and outside any regions of shear. In this case, (2.28) still holds, and allows for receptivity prediction for any distant source distribution. However, we must know the adjoint solution far from the edge (at the source location),

which may involve excessive computational expense using direct methods. In § 3.3, we show how the radiating part of the adjoint solution may be extended to large distances using a Kirchhoff surface integral formula, enabling prediction of receptivity to distant sources.

3. Receptivity of a supersonic mixing layer

3.1. *Problem set-up and numerical method*

The formulae derived for receptivity prediction based on adjoint solutions require two pieces of information: (i) a description of the regular instability wave of interest, and (ii) the relevant adjoint solution. The regular instability wave is now defined as a convectively unstable eigenmode for the non-parallel mixing layer downstream of the splitter-plate trailing edge. The details of this solution in the near-edge region are not required since the amplitude of the mode well downstream of the edge is the desired quantity. The corresponding adjoint eigenmode completes the biorthogonal eigenmode pair in the downstream region. The adjoint eigenmode, however, interacts with the splitter plate to produce a scattered adjoint field; it is this scattered field that accounts for receptivity via the edge-scattering process. The full adjoint field, denoted $\boldsymbol{V}_f^\dagger$, is a solution to the adjoint Navier–Stokes equations (2.9)–(2.11). In the present work, $\boldsymbol{V}_f^\dagger$ is obtained by finding a numerical solution to the appropriately discretized adjoint equations.

Some means of forcing the incident adjoint eigenmode is required for the numerical solution of the receptivity problem. Invoking the parallel flow assumption and considering an inviscid fluid, we may reduce the adjoint equations to an ordinary differential equation for a particular spatial eigenmode. The parallel adjoint instability mode is obtained from solution of this ODE and is introduced through forcing applied through a downstream boundary zone. The parallel eigenmode is only an approximation to the actual non-parallel adjoint instability mode, but its projection onto the actual mode is relatively large. Other modes present (for the flow conditions considered) are neutral or damped, so that the adjoint instability wave component of the solution grows and becomes the dominant 'incident' field travelling into the computational domain.

The computational domain for the adjoint field calculations, including boundary zones, is shown in figure 3. Numerical damping sponges are applied at the inflow and upper/lower computational boundaries to provide a radiation condition that absorbs the outward travelling adjoint waves. These sponge zones are based on the treatment developed by Israeli & Orszag (1981) and are characterized by a length L and strength σ. Subscripts si, so, sl and su denote the sponge parameters for the inflow, outflow, lower and upper sponges, respectively. The numerical scheme used to compute the required regular and adjoint solutions is described in detail in Barone (2003). The equations are solved in the frequency domain for a given ω using a modified five-stage Runge–Kutta scheme along with sixth-order compact finite differences. Non-trivial trailing-edge geometry, e.g. for a splitter plate of finite width, is handled by a high-order overset grid methodology. Verification of the numerical method implementation for problems of acoustic scattering and vortical disturbance generation is documented in Barone (2003).

The splitter plate consists of a rectangular section of width w capped by a rounded trailing edge. Numerical experiments with rectangular or half-plane splitter-plate shapes revealed that the singularities present at sharp corners produce unacceptable

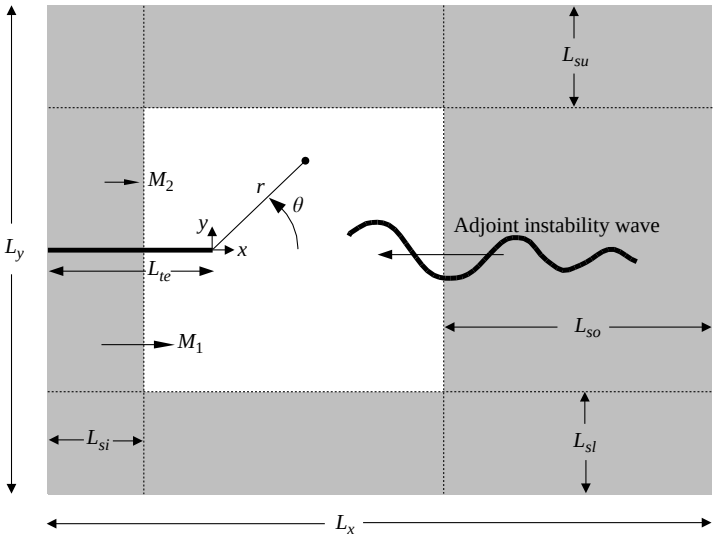

FIGURE 3. Schematic of the computational domain for the supersonic mixing-layer problem, including boundary zones (not to scale).

error levels when applying high-order centred finite-difference schemes. The symptoms of the numerical difficulties included excitation of odd–even modes at the grid Nyquist frequency that do not disappear with increasing grid resolution. The rounded trailing-edge shape, combined with the overset grid scheme outlined in Barone (2003), guarantees solution continuity and realization of the favourable convergence properties of the finite-difference scheme.

Solution of the linearized equations of motion requires a steady mean mixing-layer flow about which the flow is perturbed. The mean flow satisfies the time-independent form of the full Navier–Stokes equations. The mean flow chosen for the present study consists of a supersonic lower stream with $M_1 = 1.2$ and a small co-flow with $M_2 = 0.1$. Many applications that depend on the mixing-layer receptivity mechanism, such as jet screech and cavity oscillations, occur in the compressible flow regime, motivating the present selection of a supersonic Mach number. The non-zero co-flow was chosen to make the upper stream boundary condition unambiguous at the inflow plane, improving the iterative convergence behaviour of the base flow solution. The pressure and temperature of the two streams are equal, simulating conditions occurring in a cold pressure-matched jet. In this study, a laminar base flow is considered with superposed linear instability waves. We note that the present analysis could be extended to account for nonlinear instability wave amplitude and the attendant increase in mixing-layer growth rate by appropriate modification of the base flow.

All lengths are non-dimensionalized by the lower stream inflow boundary-layer momentum thickness θ_1^*. The numerical technique used to find the mean flow solution is very similar to the method outlined for the adjoint solutions. In this case, the inflow sponge is used to fix the boundary-layer flow on either side of the plate, with the sponge reference solution constructed from solutions of the compressible boundary-layer equations with zero pressure gradient. The method of solution for the boundary-layer equations is described in Low (1953).

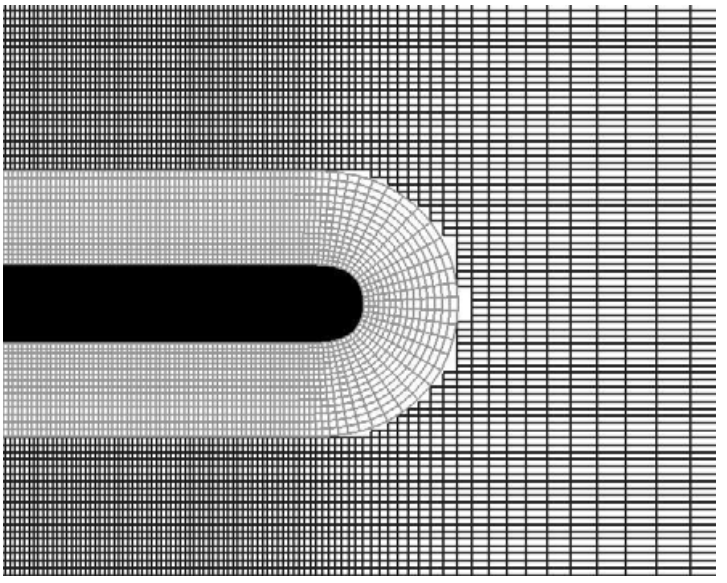

FIGURE 4. Close-up view of a typical near-edge overset grid configuration.

The chosen edge shape is a super-ellipse, which is described by the equation

$$\left(\frac{2y}{w}\right)^2 + \left(1 + \frac{x}{AR}\right)^m = 1, \qquad -AR \leqslant x \leqslant 0, \tag{3.1}$$

$$y = \pm\tfrac{1}{2}w, \qquad x < -AR, \tag{3.2}$$

where AR is the aspect ratio and m determines the level of continuity of the shape at $x = -AR$. Here we use $AR = 2.5$ and $m = 6$, which gives a relatively blunt trailing edge with a level of shape continuity consistent with the accuracy of the numerical scheme. A close-up view of the rounded edge along with a typical computational mesh structure near the edge is shown in figure 4. The plate width is chosen to be twice the boundary-layer momentum thickness θ_1, and the upper stream boundary layer has thickness $\theta_2 = \theta_1$. The Reynolds number based on θ_1^* and the lower free-stream conditions is $Re_{\theta_1^*} = 250$.

The character of the flow in the vicinity of the blunt trailing edge depends on the chosen geometry and flow parameters. Over some range of the parameters w, $\bar{u}_2/\bar{u}_1$ and $Re_{\theta_1^*}$, a global instability mode will be present, resulting in vortex-shedding in the wake behind the trailing edge. Although this phenomenon is interesting in its own right, we are focused primarily on the generation of convective instabilities in the mixing layer, independent of such vortex-shedding modes. For the flow conditions used in the present study, the near-edge flow does not possess an unstable vortex-shedding mode in the absence of a sustained excitation. This was verified by performing a numerical experiment where a pressure pulse was placed near the edge in the steady flow, setting up an initial-value problem. The full Navier–Stokes equations were then integrated for a long period of time during which the flow response near the edge was recorded. The pulse excited instabilities in the mixing layer that convected away from the edge, but oscillations near the edge were subsequently damped over time.

The required computational domain size is dictated by the largest length scales present in the problem, namely the acoustic wavelength $\lambda_a = 2\pi/\omega$, and the instability

Case	L_x	L_y	L_{te}	L_{si}	L_{so}	σ_{si}	σ_{so}
Mean1	560	400	229.5	120.9	228.1	2.0	0.5
Mean2	1050	750	382.5	234.5	500.0	2.0	0.1

TABLE 2. Domain sizes and sponge zone parameters for the supersonic mixing-layer mean flow solutions. Refer to figure 3 for domain and sponge zone length definitions.

Case	N_x	N_y	N_r	N_s	Δx_{min}	Δy_{min}	H	Δr_{min}	Δs_{min}
Mean1	700	300	40	600	0.085	0.105	4.0	0.06	0.057
Mean2	864	512	48	1120	0.117	0.105	4.0	0.06	0.057

TABLE 3. Grid parameters for the supersonic mixing-layer calculations.

wavelength $\lambda_i = 2\pi/\alpha_r$. At lower frequencies, a larger domain is required to accommodate the longer waves that populate the solution space; lower frequency leads to a computationally more expensive problem, as the near-edge region must remain well-resolved as the domain is expanded. We obtained two steady mean flow solutions, one for higher-frequency disturbance solutions and another on a larger domain for lower frequencies. The domain sizes and boundary zone parameters are given in table 2, while the relevant grid parameters are given in table 3. The Cartesian grid is composed of N_x and N_y points in the x and y directions, respectively, with non-uniform grid spacings Δx and Δy to allow for clustering of points near the trailing edge and within regions of shear. The overset grid, which extends to a constant distance H from the splitter plate, contains N_r points in the wall-normal direction and N_s points in the tangential direction. The overset grid also contains non-uniform grid spacings Δr and Δs, with clustering of points near the trailing edge.

We now describe the characteristics of the mean flow obtained on the smaller domain. Results given in the rest of this section are non-dimensionalized using the lower stream boundary-layer momentum thickness at $x = -AR$, where the flat plate joins with the super-ellipse trailing edge. This thickness, denoted θ_e^*, is a more appropriate length scale for describing the stability properties of the mixing layer. Its use as a scaling parameter is explicitly noted where it is applied, usually in the form of the ratio $\theta_e = \theta_e^*/\theta_1^*$. Figure 5 shows steady streamwise velocity profiles at three locations downstream of the splitter-plate edge. The profile just downstream of the edge is a severely asymmetric wake; further downstream the wake component 'mixes out' and the profile approximates a single-inflection-point mixing layer. Inviscid spatial linear stability theory can be used to approximate the expected bandwidth of convectively unstable frequencies supported by the mixing layer, as well as the degree of non-parallelism present. The analysis assumes a locally parallel flow and disturbances that behave like $\exp(\mathrm{i}(\omega t - \alpha x))$. Note that the presented parallel stability results are probably not good approximations to the local growth rates of actual instability mode disturbances supported by the flow; rather, they are shown to illustrate the degree of non-parallelism present and to provide a rough estimate of expected growth rates sufficiently far downstream from the edge. Figure 6(a) shows the non-dimensional spatial instability growth rate $\alpha_i\theta_e$ plotted versus real angular frequency $\omega\theta_e$ at several, nearly equally spaced, streamwise stations. Figure 6(b) shows the instability growth rate for $\omega\theta_e = 0.0815$. Both figures indicate that the stability characteristics of the steady flow profiles change rather quickly near the edge, with

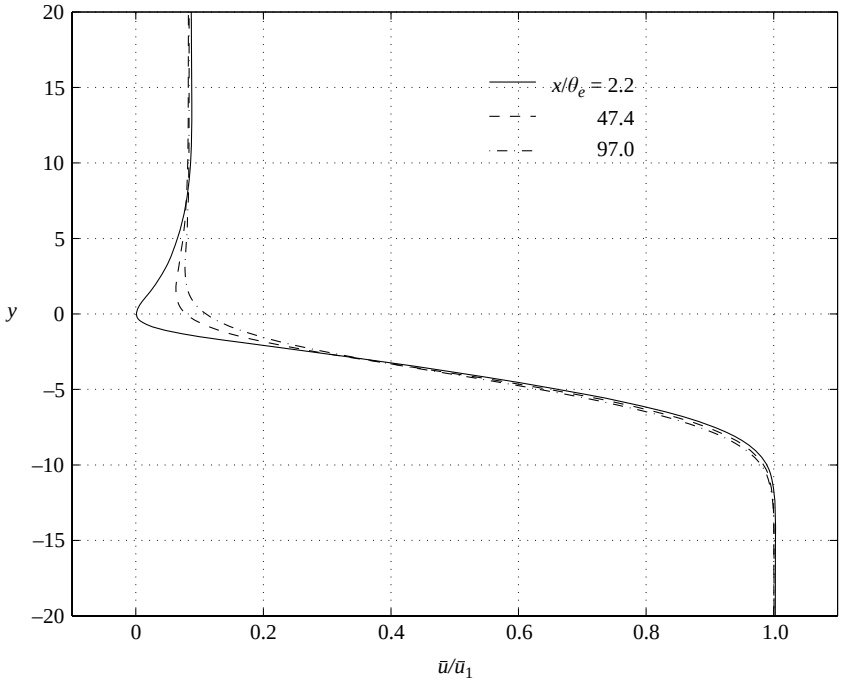

FIGURE 5. Streamwise base flow velocity profiles for three streamwise locations.

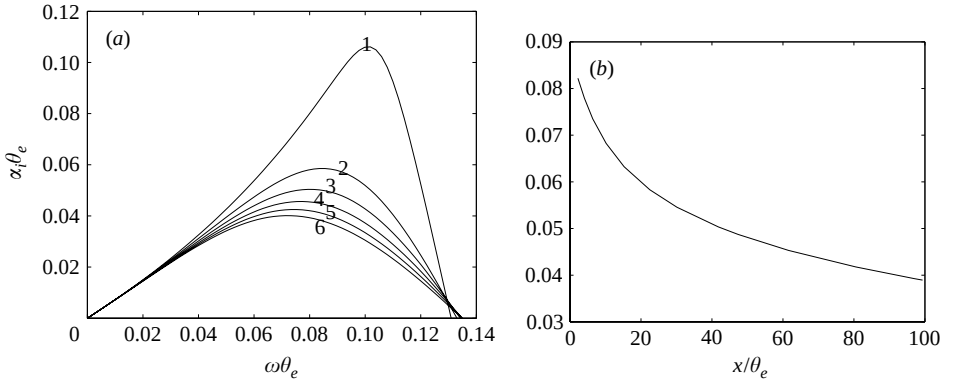

FIGURE 6. (*a*) Local instability wave growth rates based on the parallel flow approximation. $x/\theta_e = \{1 \to 2.2,\ 2 \to 22.5,\ 3 \to 41.8,\ 4 \to 61.6,\ 5 \to 80.5,\ 6 \to 99.3\}$ (*b*) Local instability wave growth rate downstream of the splitter plate edge for $\omega\theta_e = 0.0815$.

significant non-parallelism, while downstream of $x/\theta_e = 40$ or so, the flow is only weakly non-parallel.

Figure 7(*a*) depicts velocity vectors of the steady field very near the trailing edge, revealing a stagnation point close to the lower surface of the plate, and no obvious recirculation regions. The asymptotic solution found by Peake (1994) for a steady supersonic shear-layer flow past a semi-infinite plane (with stagnant upper stream) demonstrated that the region very close to the trailing edge is governed by the full

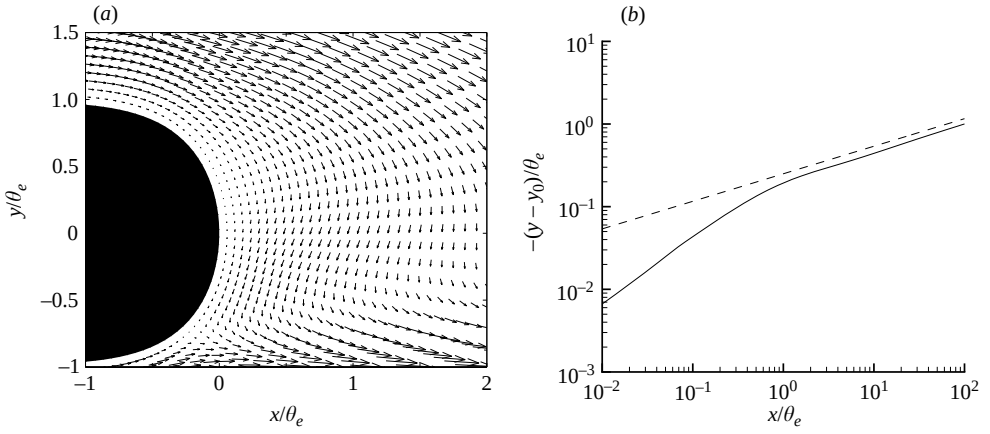

FIGURE 7. (*a*) Base flow velocity vectors near the splitter plate edge. (*b*) Behaviour of the mixing layer dividing streamline (solid line), compared to $y \sim x^{1/3}$ (dashed line). y_0 is the dividing streamline coordinate at $x = 0$.

Navier–Stokes equations, but that further away from the edge there exists a viscous wake region governed by an asymptotic solution valid for large x. One relatively simple way to compare the present computation with the predictions of the viscous theory is to examine the dividing streamline. The theory predicts a steady wake streamline shape which asymptotes to $y \sim x^{1/3}$ sufficiently far downstream of the edge. Figure 7(*b*) compares the dividing streamline from the present computation with the $x^{1/3}$ limit. The comparison is favourable despite the presence of the finite-width edge and small co-flow in the computation. The division of the dividing streamline behaviour into 'inner' and 'outer' regions suggests a way of separating the near-edge mean flow region from the slowly developing region; the transition point for asymptotic behaviour appears to occur at $x/\theta_e = 20$ or so.

3.2. *Adjoint calculation results*

In this section, we examine adjoint solutions for the supersonic splitter plate mixing-layer flow, seeking insight into the relative effectiveness of excitation by different source types and source locations, as well as identification and characterization of receptivity mechanisms.

Calculation verification

In order to examine the adjoint solutions with confidence, we must first verify the method derived for receptivity prediction in § 2.4 along with the numerical methods used to calculate the adjoint solution. This is easily done by computing a numerical solution to the forced LNS equations, then predicting the amplitude of the instability wave using the known source distribution and the adjoint solution and comparing the answers. If the numerical method is accurate for both the regular forced problem and the adjoint problem, and if (2.28) holds, then the amplitude of the excited instability wave should be predicted well by the adjoint solution.

Two such validation cases are presented here for the supersonic mixing layer. The first case involves excitation by a streamwise momentum source given by

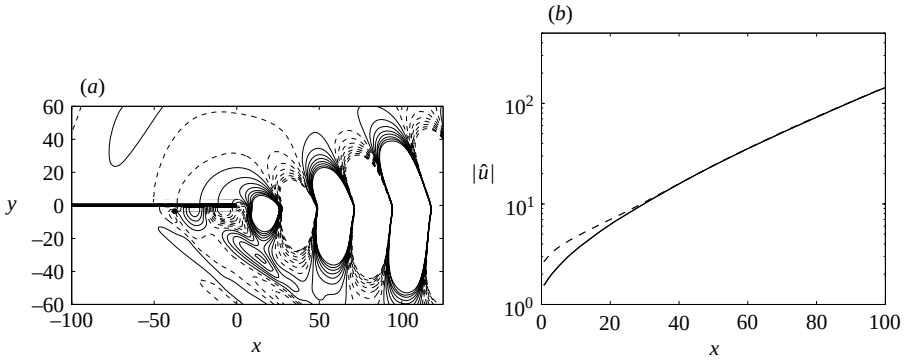

FIGURE 8. (*a*) Contours of Real$(\hat{p})$ for a streamwise momentum source (marked by a black dot) placed in the lower stream boundary layer at $(x, y) = (-37.5, -3.5)$. There are 16 equally spaced contours over the range -0.5 to 0.5. (*b*) $|\hat{u}|$ along $y = -3$. —, computed solution. – – –, prediction based on the adjoint solution.

$\bar{\rho}\hat{s}_u = f(x, y)$, where $f(x, y)$ is the two-dimensional Gaussian shape function

$$f(x, y) = \frac{1}{2\pi\sigma_x\sigma_y} \exp\left(-\frac{1}{2}\left[\left(\frac{x - x_0}{\sigma_x}\right)^2 + \left(\frac{y - y_0}{\sigma_y}\right)^2\right]\right). \tag{3.3}$$

The source is placed within the lower stream boundary layer at $(x_0, y_0) = (-37.5, -3.5)$ with $\sigma_x = 1.0$, $\sigma_y = 0.25$, so that the source region is elongated in the x direction. The excitation frequency is $\omega = 0.08$. Figure 8(*a*) shows contours of Real$(\hat{p})$ obtained by numerical solution of the LNS equations in the frequency domain. Disturbances excited within the boundary layer propagate downstream to the trailing edge, where they transfer energy to the instability wave, which dominates the downstream field. Figure 8(*b*) shows the magnitude of the streamwise velocity perturbation near the centre of the mixing layer at $y = -3$ plotted versus streamwise distance from the trailing edge. The solid line is from the LNS calculation. The dashed line is the prediction for instability wave amplitude obtained using the adjoint solution in the following manner.

In order to compare direct solutions with the present receptivity predictions over the entire region $x > 0$, it is useful to construct the entire unstable mode of interest, even near the trailing edge. For a weakly non-parallel flow, this may be obtained by an appropriate linear stability analysis of the steady base flow. This could be done using non-parallel stability theory or by finding a solution to the parabolized stability equations (PSE) downstream of the edge. For the present case, we compute an approximate unstable mode solution where the unstable wave component is expected to dominate for most of the region $x > 0$. This 'reference solution' is calculated by placing a momentum source oriented in the y direction (a dipole) near the plate edge. The instability wave component of the reference solution dominates the field downstream of the edge except for very close to the edge. The reference solution serves as the 'eigenmode' which is then normalized by the adjoint field using (2.28), giving the dashed line prediction for instability wave amplitude downstream of the edge. Note that knowledge of the unstable mode of interest for all $x > 0$ is not required to perform a receptivity analysis using the present methods; only the behaviour for large x is required. The reference solution is introduced here only for validation and illustrative purposes.

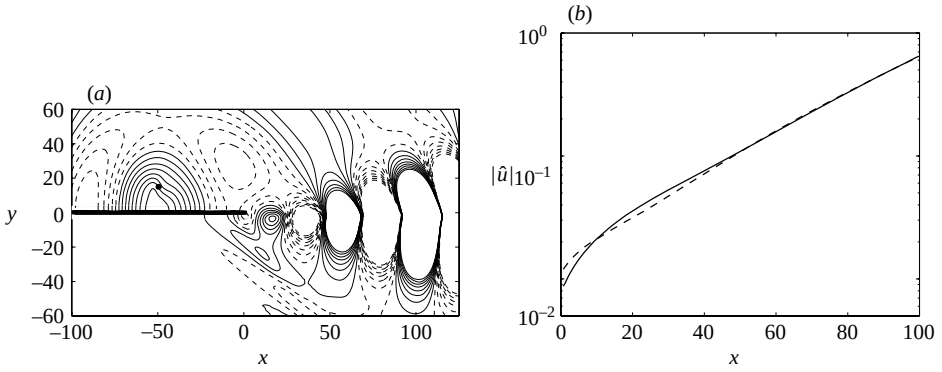

FIGURE 9. (*a*) Contours of Real($\hat{p}$) for a heat source (marked by a black dot) placed above the splitter plate at $(x, y) = (-49.5, 15)$. There are 16 equally spaced contours over the range -0.01 to 0.01. (*b*) $|\hat{u}|$ along $y = -3$. —, computed solution. – – –, prediction based on the adjoint solution.

The volume integral in (2.28) is evaluated using the trapezoidal rule applied to adjoint solution data stored at grid points. The inner product $[\hat{\boldsymbol{\phi}}, \hat{\boldsymbol{\phi}}^\dagger]$ is evaluated at the downstream edge of the physical portion of the computational domain. Figure 8 shows very good agreement between the direct calculation and the adjoint prediction. Note that the directly computed solution contains all solution modes, including damped and neutral modes. Therefore, the directly computed field deviates from the normalized instability eigenmode in the near-edge region where the eigenmode is not dominant. It is clear from comparisons further downstream, where the instability wave overwhelms other solution components, that the amplitude of the excited instability wave is correctly predicted.

Figure 9 shows results for the second test case, where a heat source oscillating at frequency $\omega = 0.08$ is placed above the plate. The prescribed source distribution is $\hat{s}_T = (1/\gamma) f(x, y)$ with f given above, and with $(x_0, y_0) = (-49.5, 15)$ and $\sigma_x = \sigma_y = 2.5$. The generated acoustic waves scatter at the trailing edge and excite the instability wave. The adjoint prediction again gives the proper instability wave amplitude to high precision. These results give confidence in the assumptions applied in the derivation of (2.28), including application of biorthogonality to a non-parallel flow. The accuracy of the receptivity prediction demonstrates that the adjoint field is sufficiently resolved and the numerical solutions satisfy the continuous Euler–Lagrange identity (2.6) to a high degree of accuracy.

The adjoint near field

Having established that the adjoint solution adequately defines the sensitivity of the mixing layer to external forcing, we may now examine the details of the adjoint solution itself. A series of adjoint computations were performed for the supersonic mixing layer where the excitation frequency was varied across the unstable range. The computational parameters for this study are presented in table 4.

Contours of the modulus of the adjoint field for $\omega = 0.04$ are plotted on a logarithmic scale in figures 10 and 11. Each adjoint field component is normalized by the maximum modulus of that component found in the computational domain. The adjoint field in the mixing-layer region is dominated by the forced adjoint instability wave, which grows exponentially in the upstream direction. Upon impinging on the splitter-plate edge the adjoint instability wave scatters, creating a complicated

ω	Mean flow	L_{si}	L_{so}	L_{sl}	L_{su}	σ_{si}	σ_{so}	σ_{sl}	σ_{su}
0.04	Mean2	234.5	500.0	169.3	169.3	0.4	3.0	0.4	0.4
0.06	Mean2	234.5	500.0	169.3	169.3	0.4	3.0	0.4	0.4
0.08	Mean1	120.9	228.1	98.6	98.6	0.4	3.0	0.2	0.2
0.10	Mean1	120.9	228.1	98.6	98.6	0.4	3.0	0.4	0.4
0.12	Mean1	120.9	228.1	98.6	98.6	0.4	3.0	0.4	0.4

TABLE 4. Boundary-zone parameters for the supersonic mixing-layer adjoint calculations.

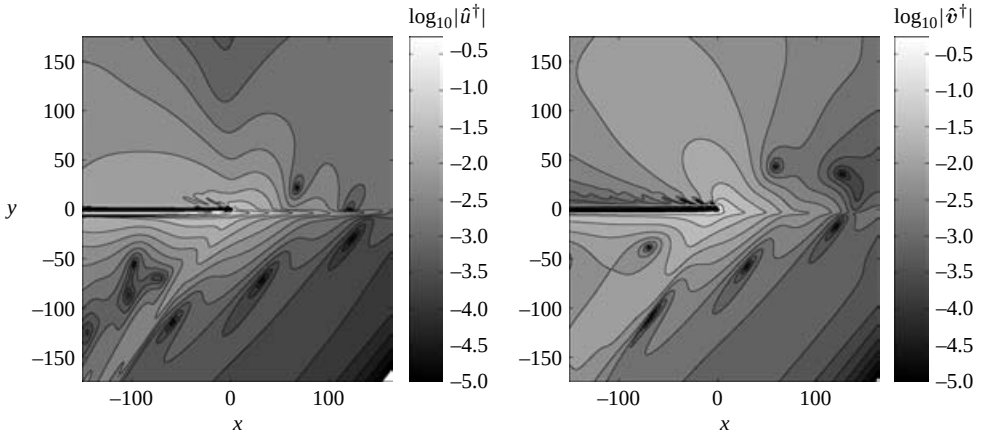

FIGURE 10. Modulus of the adjoint streamwise velocity and adjoint transverse velocity field for the supersonic mixing layer, $\omega = 0.04$.

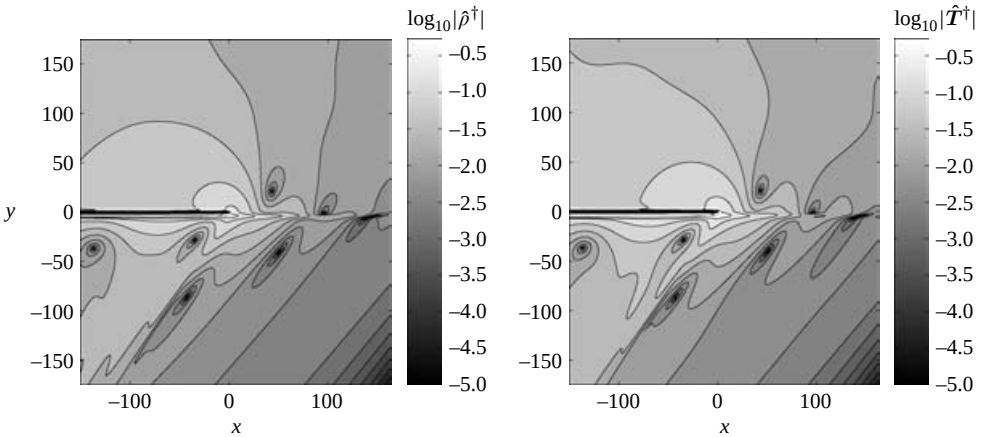

FIGURE 11. Modulus of the adjoint density and adjoint temperature field for the supersonic mixing layer, $\omega = 0.04$.

total field resulting from the superposition of the incident and scattered fields. The adjoint field within the lower (supersonic) stream boundary layer remains quite strong, decaying away from the boundary layer; this is not obvious in the figure due to the resolution of the plots, but this region is examined in detail later in this section.

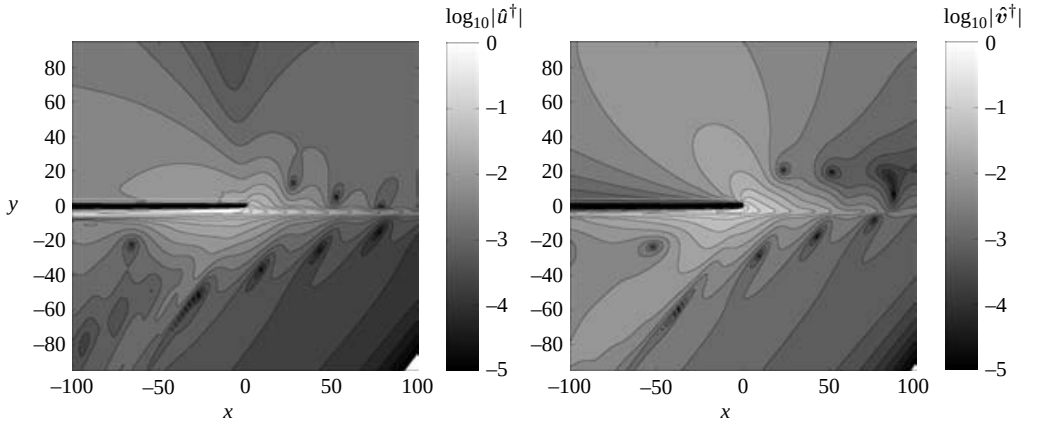

FIGURE 12. As figure 10 but for $\omega = 0.08$.

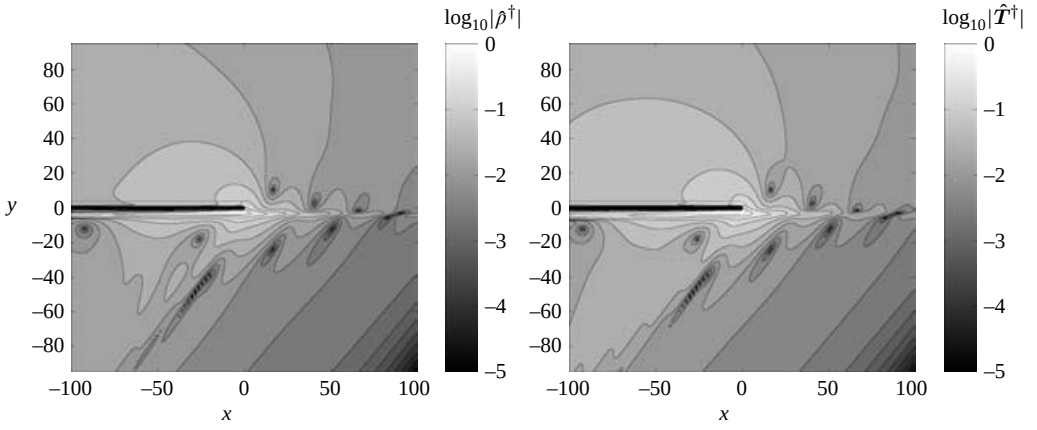

FIGURE 13. As figure 11 but for $\omega = 0.08$.

Away from the areas of mean shear are regions of very low receptivity, or nodes, in the adjoint field. The number and location of the nodes depends on the adjoint field variable, and thus on the source type. We will comment more on the physical reason for the presence of these receptivity nodes later in this section. The scattered adjoint field also presents a distinct directivity pattern related to the receptivity to acoustic waves that scatter at the trailing edge. The nature of the directivity depends on source type, but a feature common to all source types is the alignment of contours along adjoint Mach lines (which are oriented at the usual Mach angle for the reversed mean flow) within the supersonic flow at large x. This part of the adjoint field is relatively weak, and represents the acoustic receptivity path originating from an acoustic source placed in the supersonic stream. Sound radiated from the source propagates across the mixing layer, then travels upstream on the subsonic side of the mixing layer and arrives at the trailing edge where it triggers the instability wave.

Figures 12, 13, 14 and 15 show the modulus of the adjoint field components for $\omega = 0.08$ and $\omega = 0.12$. The scattering patterns observed over the unstable frequency range are qualitively similar, although the number and location of receptivity

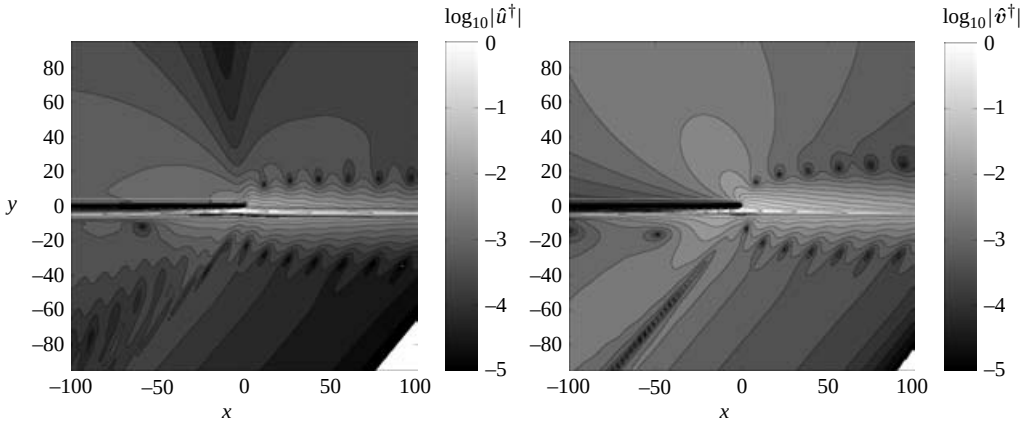

FIGURE 14. As figure 10 but for $\omega = 0.12$.

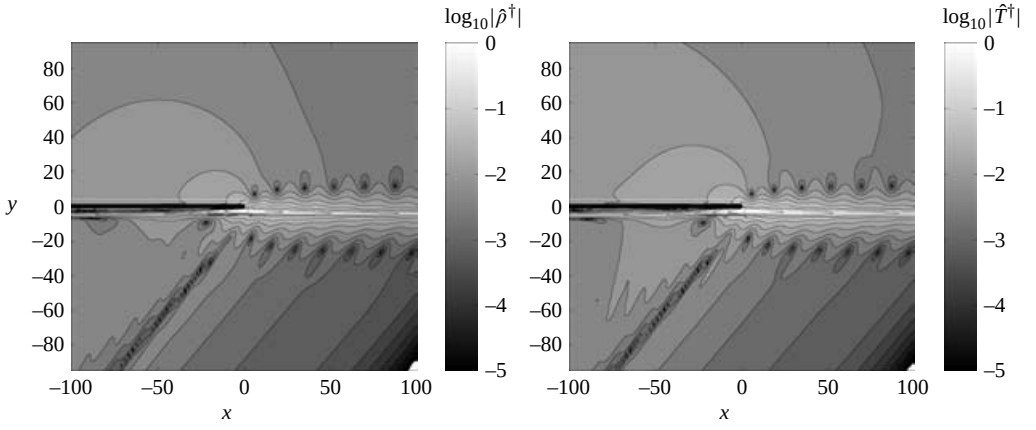

FIGURE 15. As figure 11 but for $\omega = 0.12$.

nodes vary with the frequency. The nodes downstream of the mixing layer become more aligned with the flow direction as frequency is increased. Their spacing also decreases as frequency increases, a consequence of the shrinking length scales of the problem.

Receptivity to acoustic waves may be further characterized by constructing near-field directivity plots of the adjoint field away from $y = 0$. Figure 16 shows the modulus of the adjoint field for $\omega = 0.08$ at a constant distance $r = 1.25\lambda_a$ from the trailing edge, where $\lambda_a \equiv 2\pi/\omega$ is the acoustic length scale. Data in the direct receptivity regions (regions of shear) are not displayed in the directivity plots, as their magnitude becomes much larger than values away from those regions. Above the plate, where only the small co-flow is present, streamwise momentum sources are more effective at exciting the mixing layer when placed in the upstream direction, while transverse forcing is most effective at $\theta = 120^\circ$. This is consistent with the directivity of dipole radiation observed for such sources in still air. The adjoint density and temperature correspond to monopole-like sources, whose effectiveness is seen to increase with θ above the plate. Note that in a uniform flow $\hat{\rho}^\dagger/\hat{T}^\dagger = \text{const.}$,

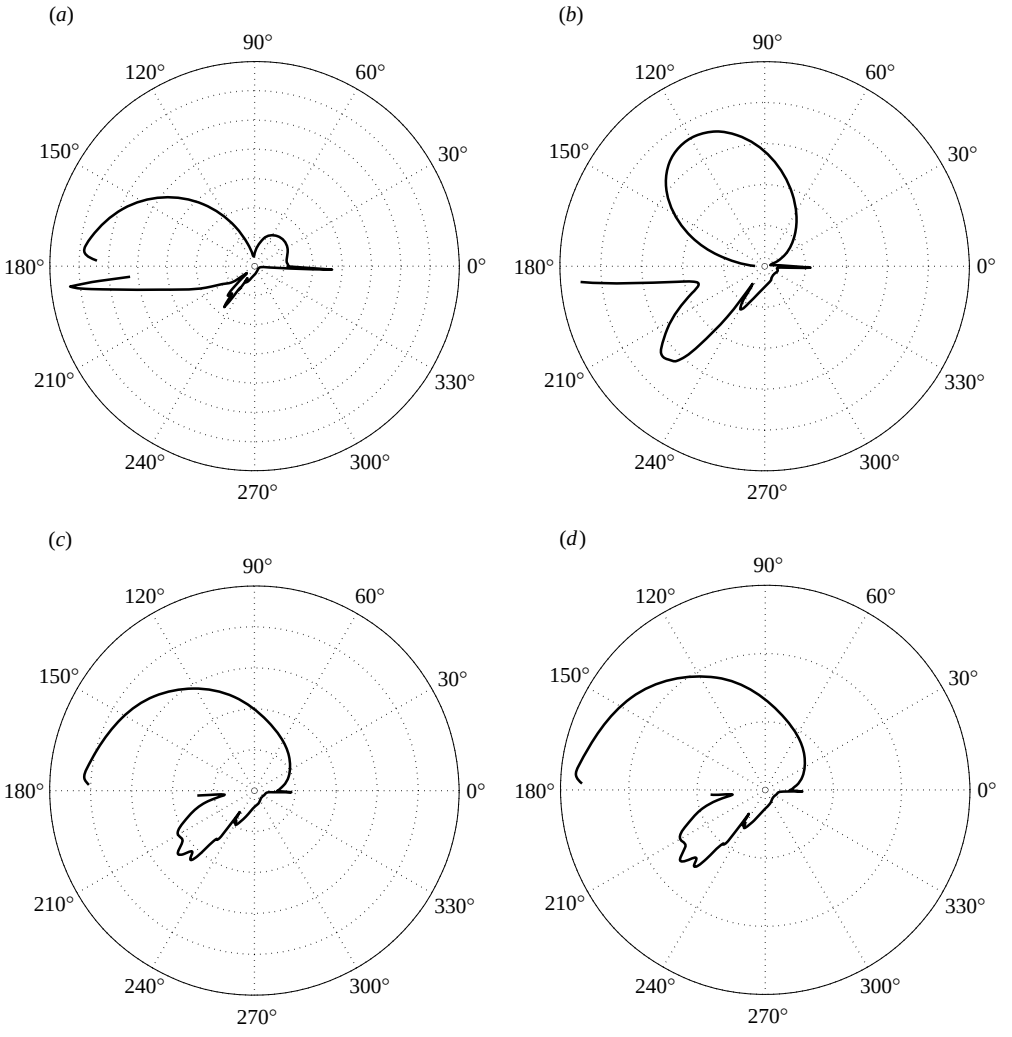

FIGURE 16. Directivity plots of the scattered adjoint field at $r/\lambda_a = 1.25$ for $\omega = 0.08$. (*a*) $|\hat{u}^\dagger|$. (*b*) $|\hat{v}^\dagger|$. (*c*) $|\hat{\rho}^\dagger|$. (*d*) $|\hat{T}^\dagger|$.

which explains the exact similarity between figures 16(c) and 16(*d*). Below the plate, a lobe of relatively strong receptivity for all source types is associated with a Mach line that intersects the trailing edge, with the adjoint streamwise velocity exhibiting a narrow peak relative to the behaviour of the other adjoint variables in that region. The directivity pattern for $\omega = 0.12$ is displayed in figure 17. The patterns are similar to the $\omega = 0.08$ case, but of note is the pronounced double lobe pattern in the supersonic stream associated with the elongated receptivity node visible in figures 14 and 15. The near-field directivity plots for $\omega = 0.04$, $\omega = 0.06$ and $\omega = 0.10$ are not shown here, but they demonstrate that the directivity pattern is a weak function of frequency, while the preferred angular source position for excitation is essentially independent of frequency. For example, the receptivity to mass sources is shown to be maximum as θ nears the upper side boundary layer at 180° for both $\omega = 0.08$ and $\omega = 0.12$, as figures 16(*c*) and 17(*c*) indicate. However, the receptivity for $\omega = 0.08$

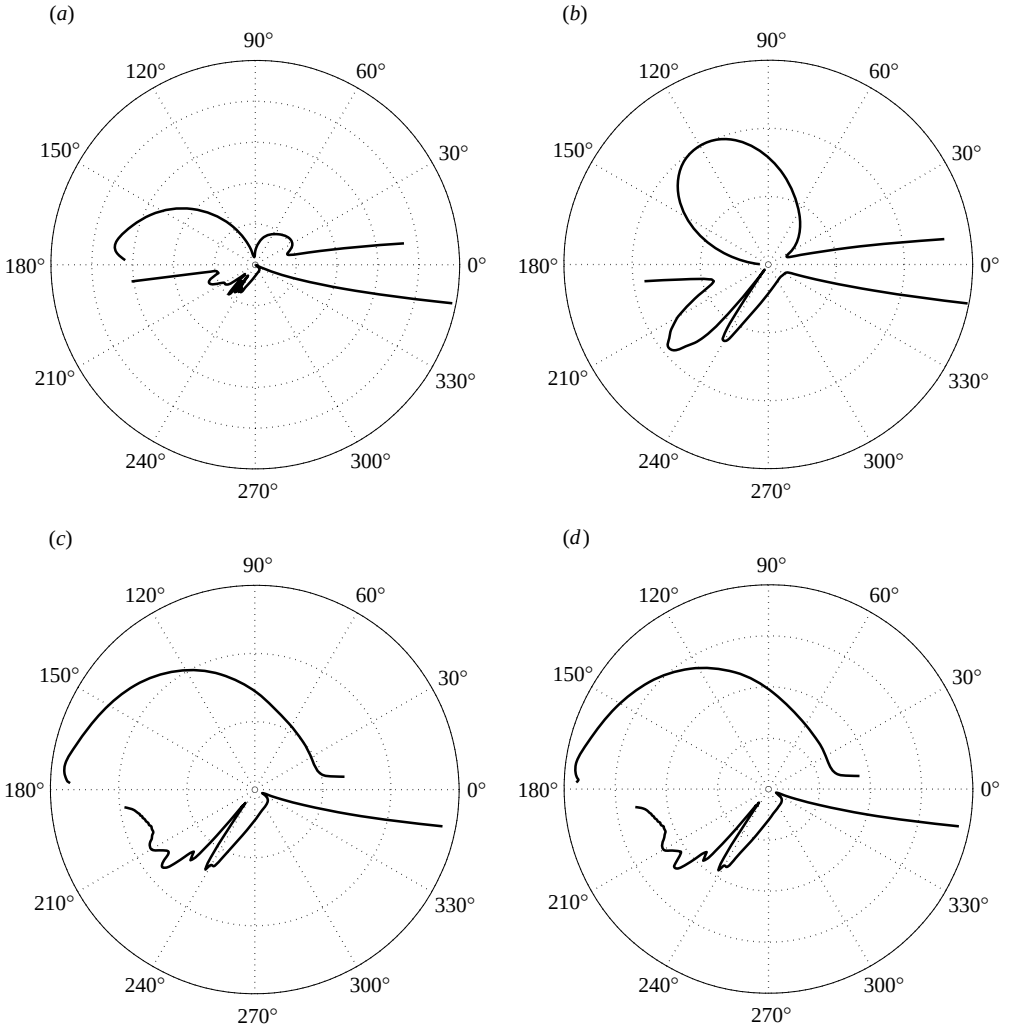

FIGURE 17. Directivity plots of the scattered adjoint field at $r/\lambda_a = 1.25$ for $\omega = 0.12$. (*a*) $|\hat{u}^\dagger|$. (*b*) $|\hat{v}^\dagger|$. (*c*) $|\hat{\rho}^\dagger|$. (*d*) $|\hat{T}^\dagger|$.

just outside the upper boundary layer is about four times stronger than at $\theta = 30°$, while for $\omega = 0.12$ the ratio is closer to 2.75.

The appearance of the receptivity nodes apparent in the contour plots of the adjoint fields prompted further analysis using the following test case. A compact momentum force, approximating a point source with frequency $\omega = 0.08$, was placed at $(x_0, y_0) = (27.5, 13)$, a location coincident with a node in the adjoint field. The response to this forcing was calculated by numerically solving the LNS equations. The source was then moved slightly downstream to $(x_0, y_0) = (38.5, 13)$, a location away from any receptivity nodes. The calculated pressure disturbance responses are shown for the two cases in figure 18, along with the adjoint receptivity predictions in figure 19. The results verify the adjoint predictions, suggesting that the receptivity nodes are real and must have a physical explanation. The presence of the nodes is explained by first noting that instability waves may be directly excited by a source,

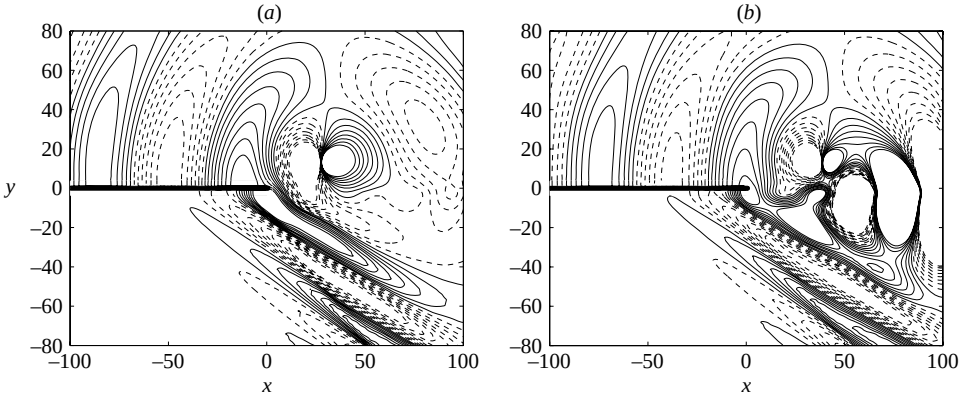

FIGURE 18. Contours of Real($\hat{p}$) for a streamwise momentum source centred at (*a*) $(x_0, y_0) = (27.5, 13)$ and at (*b*) $(x_0, y_0) = (38.5, 13)$. There are 16 equally spaced contours over the range -0.5 to 0.5.

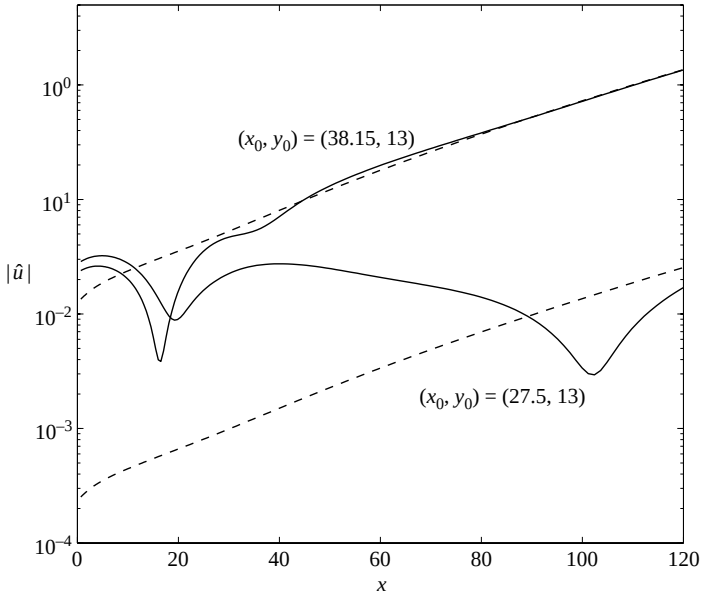

FIGURE 19. $|\hat{u}|$ along $y = -3$. —, computed solution; – – –, prediction based on the adjoint solution.

or excited when acoustic (or hydrodynamic) waves generated by the source scatter at the trailing edge. The adjoint field is comprised of a superposition of an incident instability wave field with a scattered field. The incident adjoint field is associated with direct receptivity, whereas the scattered adjoint field corresponds to receptivity via the trailing-edge scattering process. A receptivity node occurs when both mechanisms are present, each exciting an instability wave of the same magnitude, but of opposite phase, so that the sum of the two excited waves results in cancellation.

A simple model that emulates this process is constructed by taking a parallel adjoint instability mode and adding to it the field from an adjoint monopole source centred at the origin, simulating the edge-scattered field. The resulting adjoint density field for $\omega = 0.08$ is pictured in figure 20 and compared to the actual calculated field. The

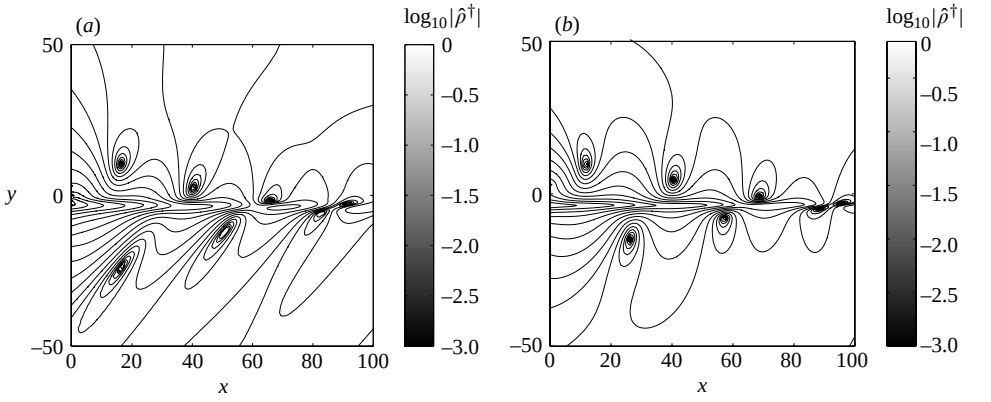

FIGURE 20. (*a*) Contours of $\log_{10}|\hat{\rho}^{\dagger}|$ for $\omega = 0.08$. (*b*) The adjoint density modulus modeled by the superposition of an instability eigenmode with an acoustic monopole field.

interference pattern is qualitatively reproduced above the plate where the mean flow is small, while below the plate the presence of the supersonic flow modifies the scattered adjoint field from a monopole distribution, and thus alters the node locations.

Predictions of this sort prove useful for interpretation of experimental results reported by Ahuja (1985). It was found that sources placed close to a jet shear layer could excite disturbances which apparently did not originate close to the jet nozzle lip, but rather further downstream near the source location. Results of this type, when interpreted alongside 'continuous coupling' theories for direct receptivity (Tam 1978; Tam & Block 1978), sparked some controversy regarding the importance of the trailing edge (Ahuja & Tam 1982). The present results conclusively support the validity of both receptivity mechanisms. The curve formed by tracing the locus of nodes in the adjoint field indicates a surface along which the trailing-edge scattering and direct receptivity mechanisms are equally effective. The fact that an acoustic scattering mechanism accounts for the nodes appearing in the downstream direction also implies that the finite thickness of the splitter plate has a significant effect on the receptivity of sources placed downstream. The vortex sheet model for receptivity, which involves a splitter plate of zero thickness, predicts exponential decay of the receptivity with increasing streamwise source location downstream of the trailing edge (Kerschen 1996). The finite-width plate thus enhances scattering of downstream-originating sound into instability waves at the trailing edge. Although we consider only the pressure-matched mixing layer in this work, this observation is consistent with the experimental work of Ponton & Seiner (1992), who found that jet screech tones could be enhanced by increasing the jet nozzle lip thickness.

3.2.1. *The lower stream boundary layer*

We now focus attention on the adjoint field within the supersonic boundary layer present on the lower edge of the plate. The adjoint instability wave does not exist upstream of the trailing edge, where there is no inflectional velocity profile that can support an inviscid instability. However, a significant portion of the 'adjoint energy' appears to be scattered into disturbances that persist in the lower stream boundary layer and propagate upstream. Figure 21 shows profiles of the modulus of the adjoint field within the lower stream boundary layer some distance upstream of the trailing edge for $\omega = 0.08$. These profile shapes are representative of the

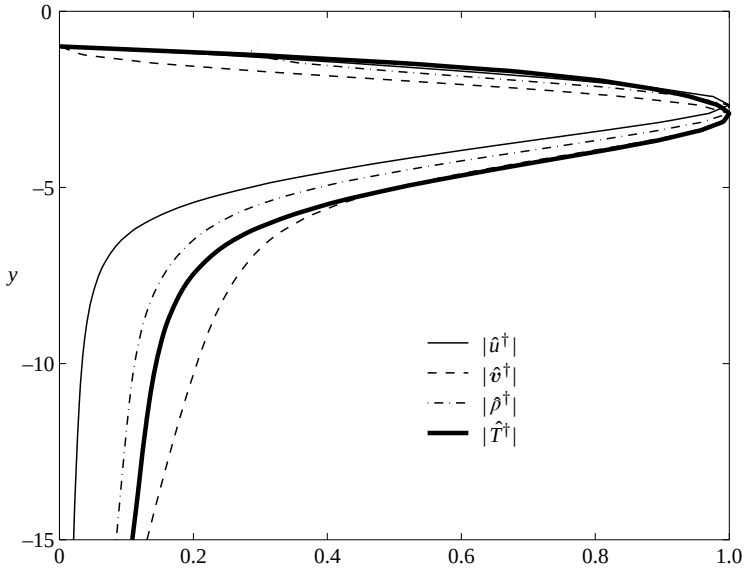

FIGURE 21. Profiles of the modulus of the adjoint field in the upstream supersonic boundary layer, normalized by the maximum profile value, at $x = -10$ for $\omega = 0.08$.

adjoint boundary–layer profiles observed for all frequencies considered. They are reminiscent of the adjoint Tollmien–Schlichting (T-S) eigenmode shapes reported by Hill (1995). The linear stability calculations of Mack (1984) indicate that for a boundary layer at $M = 1.6$ and Reynolds number $Re_{\theta_1^*} = 250$, unstable modes can exist for $0.7 \times 10^4 \leqslant \omega^* \nu^* / U_1^{*^2} \leqslant 1.6 \times 10^4$. The lowest frequency considered here, $\omega = 0.04$, corresponds to $\omega^* \nu^* / U_1^{*^2} = 1.9 \times 10^4$. It appears, then, that the frequency band for unstable T-S waves in the boundary layer coincides with a portion of the Kelvin–Helmholtz unstable frequency band that lies slightly below $\omega = 0.04$.

Figure 22 shows the maximum modulus (for a given x) of the adjoint boundary-layer field plotted versus streamwise distance from the trailing edge for four different frequencies. At each frequency, there exists a near-edge region with complicated adjoint field variation, where growth or decay of the adjoint modulus depends on the component of the solution and the frequency. The length of this region decreases with frequency until, for $\omega = 0.12$, monotonic decay away from the trailing edge of all adjoint components occurs. Outside of the near-edge region, the adjoint fields decay at a rate that is proportional to the frequency. It is likely that the solution in the boundary layer is comprised of one or more stable adjoint eigenmodes, which are associated with corresponding regular stable eigenmodes. Excitation and subsequent convection past the trailing edge of one of these regular modes provides a receptivity path for triggering the mixing layer instability mode, a fact which could prove useful in the shear flow control setting. In fact, Zaman & Hussain (1981) found that instability waves within an initially laminar jet shear layer could be effectively excited by placing an oscillating ribbon within the upstream boundary layer.

Figure 22(a) indicates that the point of maximum receptivity for mass and heat sources oscillating at $\omega = 0.04$ is located some distance upstream of the trailing edge. This boundary-layer/mixing-layer coupling mechanism may help to explain the 'anomalous' results of Parekh, Cain & Vaporean (1997), who found that a fluidic

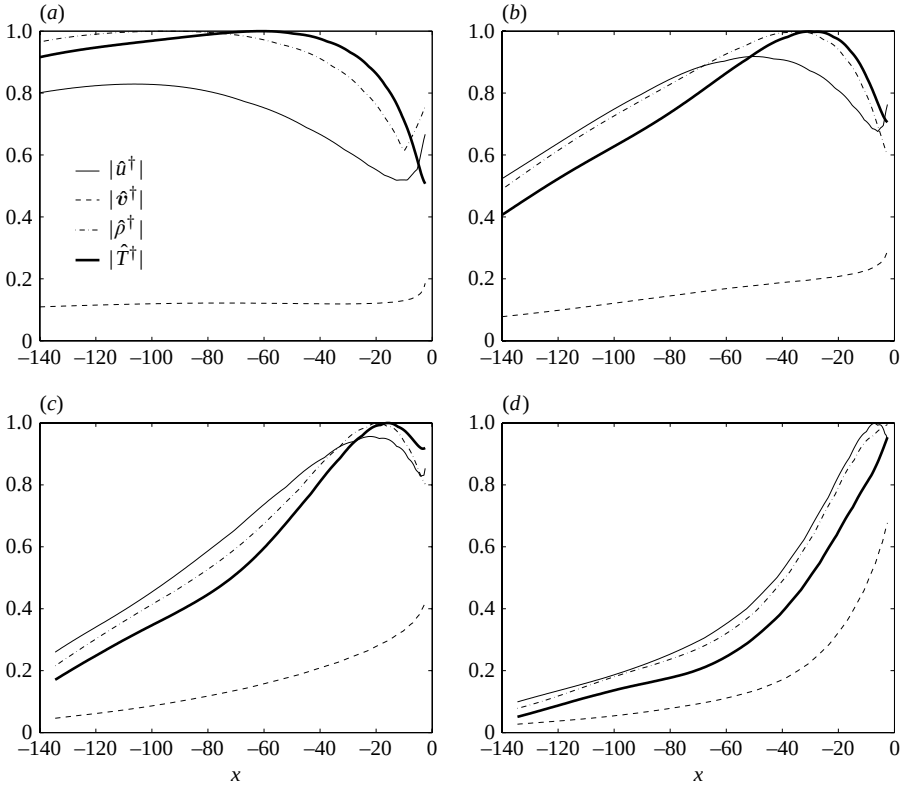

FIGURE 22. Maximum modulus of the adjoint field within the supersonic boundary layer as a function of streamwise coordinate along the splitter plate. (*a*) $\omega = 0.04$. (*b*) $\omega = 0.06$. (*c*) $\omega = 0.08$. (*d*) $\omega = 0.10$.

wall actuator placed further upstream within a jet nozzle was more effective than one placed closer to the nozzle exit.

3.3. *Far-field extension of the adjoint solution*

For certain flow configurations, one may be interested in the instability waves generated by acoustic excitation sources placed far from the edge, outside any regions of shear. Equation (2.28) certainly holds for such situations, but still requires the adjoint solution in the source region. This may pose practical problems for sources located far from the edge, as the computational domain required to directly obtain far-field adjoint solutions may become very large. A method for extracting the distant adjoint field from the solution in a computational domain of limited extent is therefore required.

The radiated adjoint solution may be found in an efficient manner using an open Kirchhoff surface. Kirchhoff surfaces have been successfully employed in many recent computational studies where a computed acoustic near field is extended to the far field (Lyrintzis 1995). A Kirchhoff integral formula relates the value of an acoustic field variable to an integral calculated over a surface completely enclosing the acoustic source region. In the present case, the Kirchhoff surface is oriented parallel to the flow direction and placed in the slow stream, allowing extension of the field above the plate. The surface is located a distance from the mixing layer such that outside of the surface the mean flow is uniform with Mach number M, and so the adjoint

density satisfies the reduced convective wave equation

$$\left[(1-M^2)\frac{\partial^2}{\partial x^2}+\frac{\partial^2}{\partial y^2}+2ikM\frac{\partial}{\partial x}+k^2\right]\hat{\rho}^\dagger=0, \tag{3.4}$$

with $\exp(-i\omega t)$ time-dependence and with $k=\omega/c$. This equation has the same form as the regular convective wave equation, a consequence of self-adjointness in the uniform flow region.

We now consider approximation of the radiated adjoint field above the plate, where the mean flow is assumed to be subsonic. The following Prandtl–Glauert variables are introduced

$$\acute{x}=\frac{x}{\sqrt{1-M^2}},\qquad \acute{y}=y,\qquad \acute{k}=\frac{k}{\sqrt{1-M^2}},\qquad \acute{\rho}=\hat{\rho}^\dagger\exp(ikMx/(1-M^2)), \tag{3.5}$$

which transforms (3.4) to the Helmholtz equation

$$\left(\frac{\partial^2}{\partial \acute{x}^2}+\frac{\partial^2}{\partial \acute{y}^2}+\acute{k}^2\right)\acute{\rho}=0. \tag{3.6}$$

The traditional Kirchhoff integral formula (see Pierce 1989, p. 181) relating a radiating solution to (3.6) at a point $\acute{\boldsymbol{x}}$ to an integral over the surface $\partial\Omega_k$ enclosing the source region is

$$\acute{\rho}(\acute{\boldsymbol{x}})=\int_{\partial\Omega_k}\left[\acute{\rho}(\acute{\boldsymbol{y}})\frac{\partial G}{\partial n}(\acute{\boldsymbol{y}}|\acute{\boldsymbol{x}})-G(\acute{\boldsymbol{y}}|\acute{\boldsymbol{x}})\frac{\partial \acute{\rho}}{\partial n}(\acute{\boldsymbol{y}})\right]\mathrm{d}S(\acute{\boldsymbol{y}}), \tag{3.7}$$

where $\partial/\partial n$ is the derivative in the direction of the outward pointing normal of the Kirchhoff surface $\boldsymbol{n}$, and G is the free-space Green's function for (3.6)

$$G(\acute{\boldsymbol{x}}|\acute{\boldsymbol{y}})=\frac{1}{4\mathrm{i}}H_0^{(2)}(\acute{k}\,|\acute{\boldsymbol{x}}-\acute{\boldsymbol{y}}|). \tag{3.8}$$

Note that the Green's function satisfies the radiation condition, which dictates that only outward travelling waves exist for $|\boldsymbol{x}|\to\infty$ as the field evolves backward in time. For (3.7) to hold exactly, the Kirchhoff surface $\partial\Omega_k$ must be closed and placed entirely in a region of the flow field which is governed by (3.6). In the present application, we use an open Kirchhoff surface consisting of all points along a line $y=h$, which terminates some distance upstream and downstream of the primary source region; thus (3.7) is used as an approximation rather than an exact relation.

Aside from the truncation error present in the near-field numerical solution, there are two main potential sources of error present when using the Kirchhoff surface technique in this fashion. The first is that the Kirchhoff surface is not closed. This error will be small provided the integration surface intersects a line connecting the source and the observer locations and $kL_k\gg 1$, where L_k is the length of the Kirchhoff surface. In this case, asymptotic correction terms may be used to reduce this source of error (Freund, Lele & Moin 1996). Any use of open Kirchhoff surfaces must be carefully validated to ensure that this error component is sufficiently small. The second source of error stems from the assumption that the Kirchhoff surface is parallel to the mean flow. In practice, the mean mixing-layer solutions contain a small transverse velocity component due to entrainment and flow expansion in the supersonic region. In the cases investigated, the maximum mean flow Mach number normal to the Kirchhoff surface is less than 0.01, introducing negligible error.

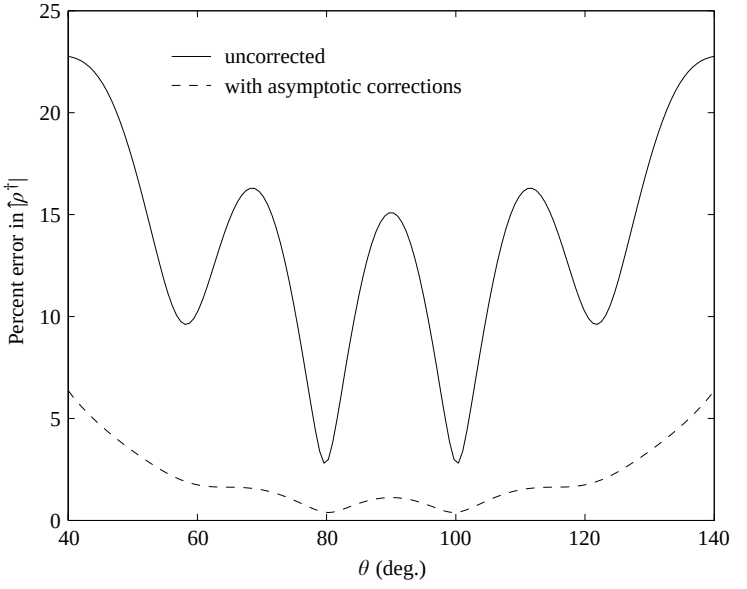

FIGURE 23. Relative error in adjoint density magnitude for the Kirchhoff prediction test problem, $r/\lambda = 45$, $k = 4.25$, $L_k = 4$, $h = 0.3025$.

3.4. *Kirchhoff surface model problem and results*

The error resulting from truncation of the Kirchhoff surface is now investigated by considering the following model problem. A stationary monopole source with $k = 4.25$ is placed in a uniform mean flow with $M = 0.1$. The source is located at $(x_0, y_0) = (0, 0)$ and we assume a computational domain in the range $-2 \leqslant x \leqslant 2$ such that a Kirchhoff surface with length $L_k = 4$ may be placed above the source at a height $h = 0.3025$. This choice of parameters gives $kL_k = 17$ and $kh = 1.29$, which is typical of the parameters used to extend the mixing-layer adjoint solutions. The adjoint density and its gradient on the Kirchhoff surface are prescribed using the exact solution for a monopole source. The solution is computed from the Kirchhoff integral relation along a circular arc of radius r extending from $\theta = 40^\circ$ to $\theta = 140^\circ$ and compared with the exact solution. Kirchhoff integral predictions are presented with and without the open surface asymptotic corrections of Freund *et al.* (1996).

Figure 23 shows the prediction error in the adjoint density amplitude versus observer angle θ for $r/\lambda_a = 50$, where $\lambda_a = 2\pi/k$. Without the correction terms, the error is quite large for this choice of parameters and is deemed unacceptable for the present application. With the correction terms, the error is less than 5 % for $45^\circ \leqslant \theta \leqslant 135^\circ$. For the present calculations, the Kirchhoff integral results give suitable data for assessing trends, if not precise numerical answers.

Figure 24 shows the modulus of the adjoint density extended to $r/\lambda_a = 50$ above the splitter plate using the calculated mixing-layer adjoint fields and a Kirchhoff surface. The Kirchhoff surface for each frequency was placed at a height above the mixing layer such that the relative error estimates from the model problem were less than 5 % over the range of angles displayed. The extended adjoint field is normalized by the maximum adjoint density modulus present in the field for the given frequency, so that the data in the figure represent the ratio of the receptivity via acoustic wave scattering to the near-edge direct receptivity for a mass source placed at the most

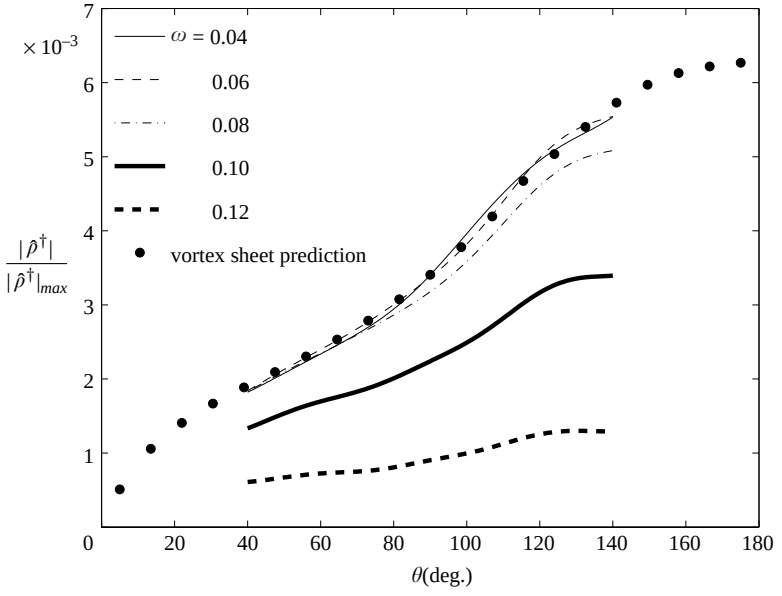

FIGURE 24. Modulus of the adjoint density extended to $r/\lambda = 50$ using a Kirchhoff surface. The adjoint density is normalized by the maximum adjoint density modulus in the field. The vortex sheet result is for $M_2 = 0$ and is normalized to match the $\omega = 0.04$ result at $\theta = 90°$.

sensitive location in the field. A low-frequency asymptote is apparent, and is consistent with the result from vortex-sheet theory with $M_2 = 0$ (Kerschen 1996). The relative acoustic receptivity decreases at higher frequencies, suggesting that the edge-scattering mechanism becomes less efficient as frequency increases outside the range of validity where an unsteady Kutta condition is obeyed (Crighton & Leppington 1974; Bechert 1988). The low-frequency regime in this case extends almost to the most unstable frequency of the downstream mixing layer, $\omega = 0.08$. Further, the receptivity to distant sources is apparently more sensitive to angular position of the source at the lower frequencies, while dependence on θ near the frequency for neutral stability is quite weak.

4. Summary and conclusions

A framework for receptivity prediction in compressible free shear flows was developed using the adjoint equation approach. The adjoint equation solutions are a direct measure of the receptivity of the flow to point source excitation of various types, and may be used to compute instability wave response to distributed sources as well. The methodology for adjoint receptivity prediction and the numerical techniques used to solve for the adjoint field were verified by comparing the adjoint predictions to regular linearized Navier–Stokes calculations of an excited mixing layer. Adjoint solutions were then obtained in the frequency domain for a mixing layer with $M_1 = 1.2$ at several frequencies spanning the frequency range containing unstable Kelvin–Helmholtz modes. The adjoint fields at all frequencies contain nodes of low receptivity that result from the interference of the incident adjoint instability mode with the edge-scattered adjoint field. We gave a physical interpretation of this

phenomenon and proposed a simple superposition model to explain the interference pattern.

Examination of the scattered adjoint field revealed zones of relatively high and low receptivity as a function of the source type and its angle measured from the downstream mixing layer. The presence of a strong adjoint field within the fast-stream boundary layer below the plate, particularly for lower frequency, indicated a receptivity mechanism that couples boundary-layer modes to the mixing-layer instability mode. Finally, we demonstrated how a Kirchhoff surface can be used to extend the scattered acoustic adjoint field to large distances, effectively giving the receptivity to incident acoustic plane wave excitation. Receptivity by acoustic scattering was shown to be more efficient relative to direct excitation of the mixing layer by a mass source as the frequency is lowered.

This work was partially supported by a Stanford Graduate Fellowship and by AFOSR grant F49620-01-1-0138. Computational resources were made available through DURIP grant F49620-01-1-0239. The authors gratefully acknowledge the improvements to the manuscript suggested by Scott Collis and Larry DeChant of Sandia National Laboratories. Sandia is a multiprogram laboratory operated by Sandia Corporation, a Lockheed Martin Company for the United States Department of Energy's National Nuclear Security Administration under contract DE-AC04-94AL85000.

Appendix. Linearized Navier–Stokes definitions

The linear viscous stress tensor appearing in (2.2) and (2.3) is given by

$$\tilde{\tau}_{ik} = \bar{\mu}\left(\frac{\partial \tilde{u}_i}{\partial x_k} + \frac{\partial \tilde{u}_k}{\partial x_i}\right) + \tilde{\mu}\left(\frac{\partial \bar{u}_i}{\partial x_k} + \frac{\partial \bar{u}_k}{\partial x_i}\right) + \left(\bar{\lambda}\frac{\partial \tilde{u}_j}{\partial x_j} + \tilde{\lambda}\frac{\partial \bar{u}_j}{\partial x_j}\right)\delta_{ik}. \tag{A 1}$$

The heat flux vector appearing in (2.3) is given by the Fourier law

$$\tilde{q}_k = -\bar{k}\frac{\partial \tilde{T}}{\partial x_k} - \tilde{k}\frac{\partial \bar{T}}{\partial x_k}. \tag{A 2}$$

The linear dissipation term appearing in (2.3) is given by

$$\tilde{\Phi} = 2\bar{\mu}\frac{\partial \bar{u}_i}{\partial x_k}\left(\frac{\partial \tilde{u}_i}{\partial x_k} + \frac{\partial \tilde{u}_k}{\partial x_i}\right) + \tilde{\mu}\frac{\partial \bar{u}_i}{\partial x_k}\left(\frac{\partial \bar{u}_i}{\partial x_k} + \frac{\partial \bar{u}_k}{\partial x_i}\right) + 2\bar{\lambda}\frac{\partial \bar{u}_i}{\partial x_i}\frac{\partial \tilde{u}_k}{\partial x_k} + \tilde{\lambda}\left(\frac{\partial \bar{u}_k}{\partial x_k}\right)^2. \tag{A 3}$$

The linearized form of the ideal gas law is

$$\tilde{p} = \frac{\gamma - 1}{\gamma}(\bar{\rho}\tilde{T} + \bar{T}\tilde{\rho}). \tag{A 4}$$

REFERENCES

Ahuja, K. K. 1985 Some unique experiments on receptivity. *AIAA Paper* 85-0533.

Ahuja, K. K. & Tam, C. K. W. 1982 A note on the coupling between flow instabilities and incident sound. *J. Sound Vib. Lett. Ed.* **83**, 433–439.

Airiau, C. 2000 Non-parallel acoustic receptivity of a Blasius boundary layer using an adjoint approach. *Flow Turb. Combust.* **65**, 347–367.

Balsa, T. F. 1988 On the receptivity of free shear layers to two-dimensional external excitation. *J. Fluid Mech.* **187**, 155–177.

Balsa, T. F. 1993 Flow generated by a small oscillating cylinder in a mixing layer. *J. Fluid Mech.* **248**, 237–265.

Barone, M. F. 2003 Receptivity of compressible mixing layers. PhD thesis, Department of Aeronautics and Astronautics, Stanford University.

Bechert, D. W. 1988 Excitation of instability waves in free shear layers. Part 1. Theory. *J. Fluid Mech.* **186**, 47–62.

Bechert, D. W. & Stahl, B. 1988 Excitation of instability waves in free shear layers. Part 2. Experiments. *J. Fluid Mech.* **186**, 63–84.

Bower, W. W. & Pal, A. 1996 Receptivity of a supersonic cylindrical jet to an acoustic wave. Part II: Numerical results. FED 236, *1996 ASME Fluids Engng Div. Conf*, vol. 2, pp. 459–463.

Brown, G. B. 1935 On vortex motion in gaseous jets and the origin of their sensitivity to sound. *Proc. Phys. Soc.* **47**, 703–732.

Crighton, D. G. 1985 The Kutta condition in unsteady flow. *Annu. Rev. Fluid Mech.* **17**, 411–445.

Crighton, D. G. & Leppington, F. G. 1974 Radiation properties of the semi-infinite vortex sheet: the initial value problem. *J. Fluid Mech.* **64**, 393–414.

Daniels, P. G. 1977 Viscous mixing at a trailing edge. *Q. J. Mech. Appl. Maths* **30**, 319–342.

Day, M. J., Mansour, N. N. & Reynolds, W. 2001 Nonlinear stability and structure of compressible reacting mixing layers. *J. Fluid Mech.* **446**, 375–408.

Dobrinsky, A. & Collis, S. S. 2000 Adjoint parabolized stability equations for receptivity prediction. *AIAA Paper* 2000-2651.

Dziomba, B. & Fiedler, H. E. 1985 Effect of initial conditions on two-dimensional free shear layers. *J. Fluid Mech.* **152**, 419–442.

Ffowcs Williams, J. E. 2001 Active flow control. *J. Sound Vib.* **239**, 861–871.

Freund, J. B., Lele, S. K. & Moin, P. 1996 Calculation of the radiated sound field using an open Kirchhoff surface. *AIAA J.* **34**, 909–916.

Hill, D. C. 1995 Adjoint systems and their role in the receptivity problem for boundary layers. *J. Fluid Mech.* **292**, 183–204.

Hill, D. C. 1997 Receptivity in non-parallel boundary layers. *ASME Fluids Engng Div. Summer Meeting*, FEDSM97-3108.

Ho, C. & Huerre, P. 1984 Perturbed free shear layers. *Annu. Rev. Fluid Mech.* **16**, 365–424.

Huerre, P. & Monkewitz, P. A. 1985 Absolute and convective instabilities in free shear layers. *J. Fluid Mech.* **159**, 151–168.

Israeli, M. & Orszag, S. A. 1981 Approximation of radiation boundary conditions. *J. Comput. Phys.* **41**, 115–135.

Jones, D. S. & Morgan, J. D. 1972 The instability of a vortex sheet on a subsonic stream under acoustic radiation. *Proc. Camb. Phil. Soc.* **72**, 465–488.

Jones, D. S. & Morgan, J. D. 1973 The instability due to acoustic radiation striking a vortex sheet on a supersonic stream. *Proc. R. Soc. Edin. A* **71**, 121–140.

Kerschen, E. J. 1996 Receptivity of shear layers to acoustic disturbances. *AIAA Paper* 96-2135.

Ling, C. H. & Reynolds, W. C. 1973 Non-parallel flow corrections for the stability of shear flows. *J. Fluid Mech.* **59**, 571–591.

Low, G. M. 1953 The compressible laminar boundary layer with heat transfer and small pressure gradient. *NACA TN* 3028.

Luchini, P. & Bottaro, A. 1998 Görtler vortices: a backward-in-time-approach to the receptivity problem. *J. Fluid Mech.* **363**, 1–23.

Lyrintzis, A. S. 1995 Review: the use of Kirchhoff's method in computational aeroacoustics. *J. Fluids Engng* **116**, 665–676.

Mack, L. M. 1984 Boundary layer linear stability theory. Special course on stability and transition of laminar flow *AGARD-R*-709. pp. 3.1–3.81.

Morgan, J. D. 1974 The interaction of sound with a semi-infinite vortex sheet. *Q. J. Mech. Appl. Maths* **27**, 465–487.

Morkovin, M. V. & Paranjape, S. V. 1971 On acoustic excitation of shear layers. *Z. Flugwiss.* **19**, 328–335.

Munt, R. M. 1977 The interaction of sound with a subsonic jet issuing from a semi-infinite cylindrical pipe. *J. Fluid Mech.* **83**, 609–640.

Noble, B. 1958 *Methods Based on the Wiener–Hopf Technique*. Pergamon.

Pal, A. 1996 Receptivity of a supersonic cylindrical jet to an acoustic wave. Part I: Solution based on the Wiener–Hopf technique. FED 236. 1996 Fluids Engng. Div. Conf.

Parekh, D. E., Cain, A. B. & Vaporean, C. N. 1997 Characterization of receptivity in jet flow control. AFOSR TR-97-0724, McDonnell Douglas.

Peake, N. 1994 The viscous interaction between sound waves and the trailing edge of a supersonic splitter plate. *J. Fluid Mech.* **264**, 321–342.

Pierce, A. D. 1989 *Acoustics: An Introduction to its Physical Principles and Applications*. Acoustical Society of America.

Ponton, M. K. & Seiner, J. M. 1992 The effects of nozzle exit lip thickness on plume resonance. *J. Sound Vib.* **154**, 531–549.

Rabchuk, J. A. 2000 Receptivity to harmonic forcing of a finite-width mixing layer just downstream of the trailing edge of a flat plate. *Phys. Fluids* **12**, 1749–1761.

Raman, G. & Kibens, V. 2001 Active flow control using integrated powered resonance tube actuators. *AIAA Paper* 2001–3024.

Salwen, H. & Grosch, C. E. 1981 The continuous spectrum of the Orr–Sommerfeld equation. Part 2. Eigenfunction expansions. *J. Fluid Mech.* **104**, 445–465.

Saric, W. S. & Nayfeh, A. H. 1975 Nonparallel stability of boundary layer flows. *Phys. Fluids* **18**, 945–950.

Stanek, M. J., Raman, G., Kibens, V., Ross, J. A., Ohedra, J. & Peto, J. W. 2000 Control of cavity resonance through very high frequency forcing. *AIAA Paper* 2000-1905.

Suzuki, T. 2001 Acoustic wave propagation in transversely sheared flows. PhD thesis, Department of Aeronautics and Astronautics, Stanford University.

Tam, C. K. W. 1978 Excitation of instability waves in a two-dimensional shear layer by sound. *J. Fluid Mech.* **89**, 357–371.

Tam, C. K. W. 1986 Excitation of instability waves by sound – a physical interpretation. *J. Sound Vib. Lett. Ed.* **105**, 169–172.

Tam, C. K. W. & Aurialt, L. 1998 Mean flow refraction effects on sound radiated from localized sources in a jet. *J. Fluid Mech.* **370**, 149–174.

Tam, C. K. W. & Block, P. 1978 On the tones and pressure oscillations induced by flow over rectangular cavities. *J. Fluid Mech.* **89**, 373–399.

Tam, C. K. W. & Morris, P. J. 1985 Tone excited jets, Part V: A theoretical model and comparison with experiment. *J. Sound Vib.* **102**, 119–151.

Tumin, A. M. & Fedorov, A. V. 1983 Excitation of unstable waves in boundary layer on a vibrating surface. *J. Appl. Mech. Tech. Phys.* **24**, 348–354.

Tumin, A. M. & Fedorov, A. V. 1984 Instability wave excitation by a localized vibrator in the boundary layer. *J. Appl. Mech. Tech. Phys.* **25**, 867–873.

Wiltse, J. M. & Glezer, A. 1998 Direct excitation of small-scale motions in free shear flows. *Physics of Fluids* **10**, 2026–2036.

Zaman, K. B. M. Q. & Hussain, A. K. M. F. 1981 Turbulence suppression in free shear flows by controlled excitation. *J. Fluid Mech.* **103**, 133–159.